Mechanism studies of seasonal variability of dissolved oxygen in Mass Bay: A multi-scale FVCOM/UG-RCA application

Pengfei Xue [a,*], Changsheng Chen [b,d], Jianhua Qi [b], Robert C. Beardsley [c], Rucheng Tian [b], Liuzhi Zhao [b], Huichan Lin [b]

[a] Department of Civil and Environmental Engineering, Great Lake Research Center, Michigan Technological University, Houghton, MI 49931, United States
[b] School for Marine Science and Technology, University of Massachusetts-Dartmouth, New Bedford, MA 02744, United States
[c] Department of Physical Oceanography, Woods Hole Oceanographic Institution, Woods Hole, MA 02543, United States
[d] International Center for Marine Studies, Shanghai Ocean University, Shanghai, PR China

ARTICLE INFO

ABSTRACT

Long-term (1992–2010) water quality monitoring records reveal that the dissolved oxygen (DO) concentration in Mass Bay exhibits a well-defined seasonal cycle, highest in March–April and lowest in October. This pattern persists in all years with insignificant interannual variability. A multi-domain-nested coupled physical–biogeochemical model was developed and applied to simulate the DO field over the 16-year period 1995–2010. The model-computed DO and nitrogen concentrations were in good agreement with observations. An EOF analysis of the modeled DO field indicates that DO in Mass Bay features both well-defined seasonal and spatial modes. The magnitude and phase of the DO seasonal cycle vary more significantly in the southern bay than in the northern bay. Horizontal advection, which is connected to the western Gulf of Maine coastal currents, plays a dominant role in the DO variability in the northern bay. The southern bay features a well-defined local retention mechanism with a longer residence time. In this region, the DO variation is controlled predominantly by local biogeochemical processes. Since the photosynthetic minus respiration production of DO is always balanced to a large degree by the oxidation of organic matters, reaeration becomes a major driver for the seasonal cycle of DO.

© 2013 Elsevier B.V. All rights reserved.

1. Introduction

Mass Bay is referred here to the *entire* semi-enclosed embayment system formed by Massachusetts Bay (MB) between Cape Ann and Race Point and Cape Cod Bay (CCB) (south of Race Point), in the western Gulf of Maine (Fig. 1). The water depth in this bay ranges from a few meters near the coast to more than 90 m near the boundary. The major circulation in Mass Bay features an anti-clockwise gyre with an inflow from the upstream north near Cape Ann and an outflow through the south passage near the tip of Cape Cod (Bigelow, 1927; Geyer et al., 1992). The inflow is a continuous branch of the Western Maine Coastal Current (WMCC) together with freshwater discharge from the Merrimack River. After entering northern Mass Bay this flow separates into two branches: one moves southward along the local isobaths extending into CCB and another branch moves southeastward towards the southern outflow passage (Fig. 1). Inside CCB in the south, the water generally flows along the 20–40 m isobaths.

Over the last two decades, the Mass Bay ecosystem has experienced remarkable changes: increased outbreaks of harmful algal blooms (Anderson et al., 2005, 2007); the long-term shift of phytoplankton species and increased (decreased) occurrences of the spring (fall) blooms (Hunt et al., 2010); dramatic decrease of *anadromous* fishes (e.g. blueback herring) (Reback et al., 2004); and the restoration of water quality after relocation of the sewage outfall from Boston Harbor to MB (Oviatt et al., 2007; Signell et al., 2000). Dissolved oxygen (DO), one of the primary state variables used for water quality assessment, has received extensive public and governmental attention. Although no observations have shown that DO concentration minima in Mass Bay led towards hypoxia or anoxia, insufficient oxygen in the water column can cause a shift of aquatic species, and a decrease of feeding, reproductive and spawning activities of aquatic animals and thus threatens ecosystem health.

There has been long-term DO monitoring in Mass Bay since the 1990's. These data showed a well-shaped seasonal cycle of DO in Mass Bay with the highest concentration during spring and lowest concentration during autumn (Fig. 2). This seasonal variation pattern has remained relatively steady over the last 18 years, with an interannual variation of only ~10% near the surface and bottom. Unlike DO, other primary state variables exhibited considerable interannual variability. For example, the dissolved inorganic nitrogen concentration varied interannually in a range up to 40% near the surface and 60% near the bottom. The chlorophyll-a concentration, an indicator of phytoplankton biomass, showed extreme change during spring and fall blooms, with an interannual variation up to 120% near the surface and 110% near the bottom.

---

* Corresponding author at: Michigan Technological University, 1400 Townsend Dr., Building GLRC-317, Houghton, MI 49931, United States.
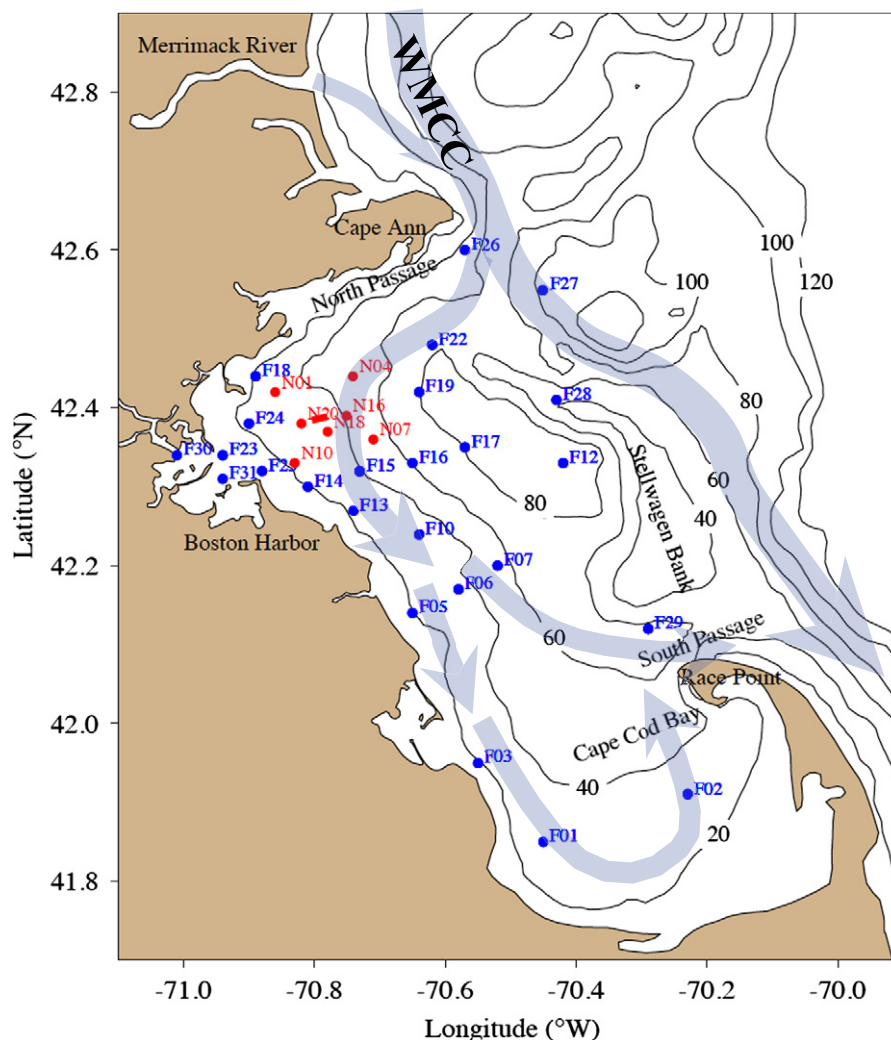*E-mail address:* pexue@mtu.edu (P. Xue).

Fig. 1. Bathymetry of Mass Bay (MB) and adjacent regions. Nearfield (red dots) and farfield (blue) denote water quality stations sampled in MB by the MWRA Outfall Monitoring Program. "MB" in this paper refers to the entire semi-enclosed embayment system formed by Massachusetts Bay (between Cape Ann and Race Point) and Cape Cod Bay (south of Race Point). Schematics of the mean flow patterns suggested by previous studies (Bigelow, 1927; Geyer et al., 1992) are overlaid. The inflow is primarily determined by the bifurcation and intrusion of the Western Maine Coastal Current (WMCC) and coastal freshwater discharges (mainly from the Merrimack River).

The distinct interannual variability exhibited by DO and other water quality variables raises a fundamental question: what are the key mechanisms controlling the seasonal and interannual variability of DO in Mass Bay? The DO concentration is controlled by physical and biogeochemical processes, including water transport, water stratification and mixing, air–sea interaction (reaeration), photosynthesis, respiration, oxidation of organic matter, and sediment oxygen demand (SOD). The relatively small interannual variability of DO concentration observed at monitoring sites in Mass Bay, however, suggests that there must be dominant processes or a dynamical balance among these physical and biogeochemical processes over an annual scale. Which processes are dominant and what balance could it be? These questions, to our knowledge, have not been well explored yet.

Kelly and Doering (1999) used a 1-D conceptual model to examine the influence of seasonal variability of water stratification on DO in MB. Their results suggest that the seasonal deepening of the pycnocline forms an isolated thin layer near the bottom. In this layer, the increase of sediment respiration can cause the decline of DO concentration. Geyer et al. (2002) used a statistical regression model to examine the seasonal and annual trends of DO in MB. His model shows that the variability of DO in MB is a regional phenomenon that is related to the upstream inflow. Jiang et al. (2007) investigated the formation of high nutrients

and low oxygen (HNLO) concentrations near the bottom in CCB during the summer of 2000. Their model results suggest that in the summer, HNLO concentrations could be formed as a result of intensive regeneration and accumulation of nutrients beneath the thermocline. All of these DO-related modeling studies, however, were focused on either a specific year or a particular sub-region of Mass Bay, and no studies to our knowledge have been carried out to examine physical and biogeochemical processes that control the seasonal and interannual variability of DO in Mass Bay.

We have developed an eutrophication model for Mass Bay and applied it to simulate the DO concentration for the period 1995–2010. The model results were first validated by comparison with field measurement data, and then used to examine the processes controlling the temporal and spatial variabilities of DO in this region. An EOF (Empirical Orthogonal Function) analysis was conducted to characterize dominant modes of DO and process-oriented diagnostic numerical experiments were made to verify the key mechanism causing its interannual variability.

The remaining sections of this paper are organized as follows. In Section 2, the model, data and design of numerical experiments are described. In Section 3, both observed and model-computed fields are presented, with inclusion of model-data comparisons. In Section 4, the
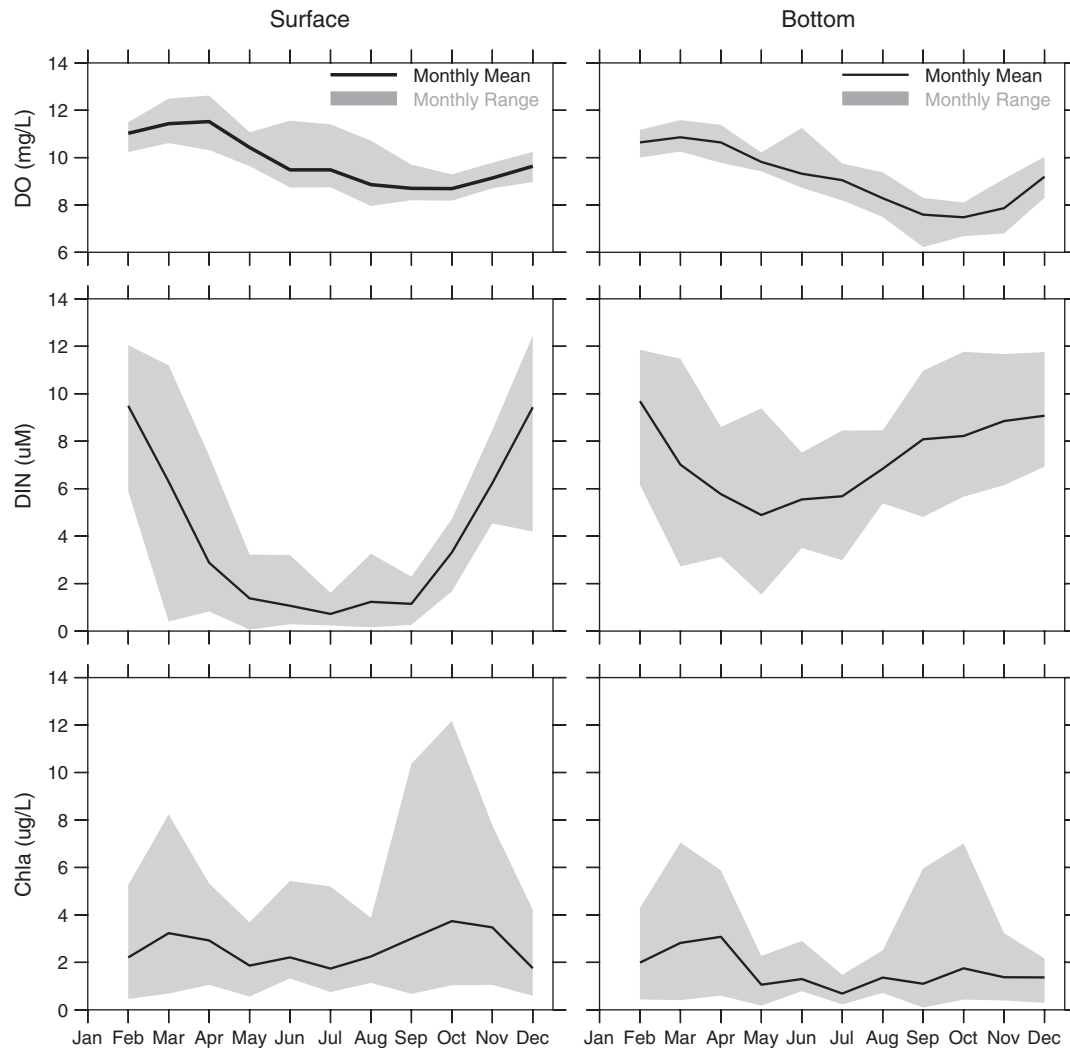
Surface

Bottom

Fig. 2. Time series of monthly means of dissolved oxygen (DO) concentration (upper), dissolved inorganic nitrogen (DIN) concentration (middle), and chlorophyll-a concentration (Chl-a) (lower) near the surface (left) and near the bottom (right) averaged over the period 1992–2010. Gray shadow areas indicate the interannual variability.

dominant EOF DO temporal and spatial modes are presented. In Section 5, key mechanisms controlling the temporal/spatial variability of DO and the balance of DO fluxes from individual biogeochemical processes are discussed. Conclusions are summarized in Section 6.

2. Methods and approaches

2.1. The Mass Bay-FVCOM/UG-RCA model

Mass Bay-FVCOM is a subdomain FVCOM (Chen et al., 2003; C.R.C. Chen et al., 2006a; C.G. Chen et al., 2006b) that is nested within the regional Gulf of Maine (GoM) FVCOM (hereafter referred to as GoM-FVCOM) (Fig. 3). The computational domain of Mass Bay-FVCOM is configured with a non-overlapped triangular mesh, with a horizontal resolution varying from 0.3 to 0.5 km inside Boston Harbor to 9.0 km off the coast near the nesting boundary. Both Mass Bay-FVCOM and GoM-FVCOM use the same hybrid vertical coordinate (Pietrzak et al., 2002), in which the water column is divided into 30 layers and the resolution is 1.0 m or less in the shallow regions. Mass Bay-FVCOM is driven by atmospheric forcing (wind stress, surface heat flux/shortwave irradiance, precipitation minus evaporation), freshwater discharge from rivers and nested boundary forcing output from GoM-FVCOM. The atmospheric forcing used here is the assimilated hindcast field of the GoM-Weather Research and Forecast (WRF) model, which was configured for the Northeast Coastal Ocean Forecast System (NECOFS). The

river runoff data are obtained from the USGS monitoring sites in each river. GoM-FVCOM has been run from 1995 to present, with inclusion of assimilation of the satellite-derived sea surface temperature, and temperature/salinity profile data from available buoys and field surveys. GoM-FVCOM includes five (M_2, N_2, S_2, K_1 and O_1) tidal constituents so that the tidal motion in Mass Bay-FVCOM is generated through the nesting boundary connected to GoM-FVCOM.

Mass Bay-FVCOM and GoM-FVCOM used the same numerical algorithms, which are described in detail in the FVCOM user's manual (Chen et al., 2006b). In this study, both local and regional models use the Mellor and Yamada (1982) level 2.5 turbulence closure submodel for vertical mixing parameterization. The horizontal diffusion is simulated using the Smagorinsky (1963) formulation in which the diffusion is a function of model resolution and horizontal current shear.

UG-RCA is the unstructured-grid version of the Row-Column Advanced (RCA) water quality model. The RCA water quality model was originally developed for Mass Bay in the early 1990s and is coupled with the structured-grid hydrodynamic model ECOM-si (Blumberg, 1994; HydroQual, Inc., 2003; HydroQual, Inc. and Normandeau Associates, 1995; Jiang and Zhou, 2004; Jiang et al., 2007; Signell et al., 2000; Tian et al., 2009). In 2006, the physical model ECOM-si was replaced by FVCOM for its merits of accurately resolving the complex geometry and local bathymetry in Mass Bay. For consistency, the RCA water quality model was updated to its unstructured-grid version (UG-RCA) to ensure local mass conservation in the coupling between
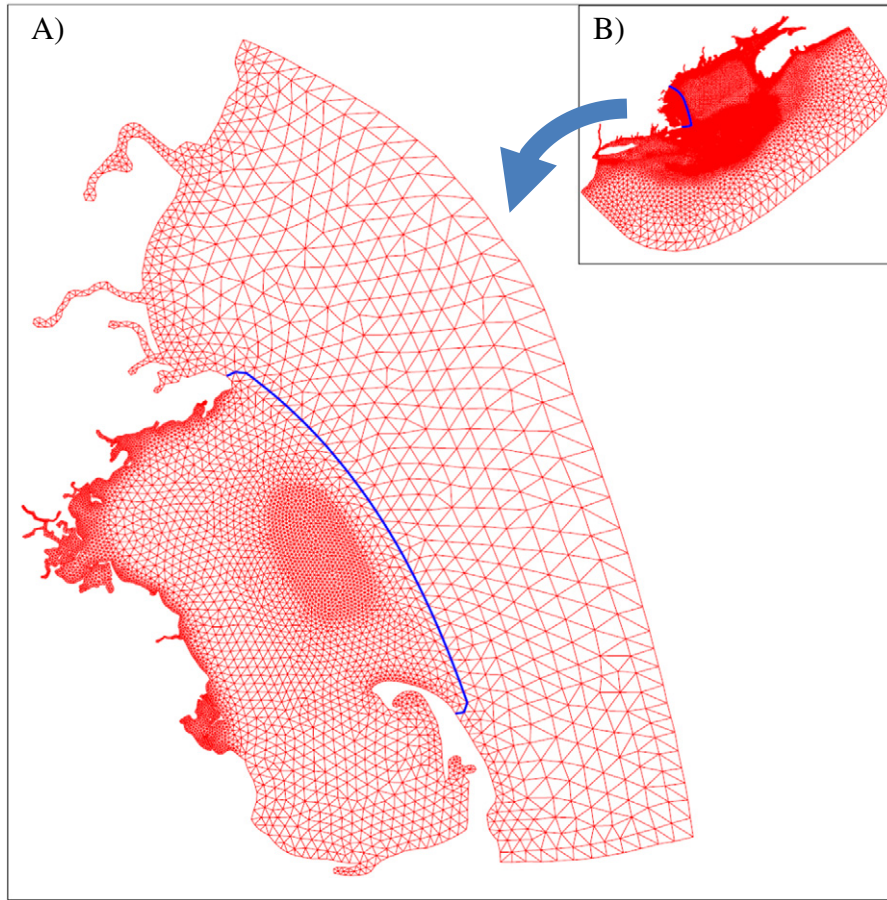
Fig. 3. Unstructured grid of Mass Bay-FVCOM (panel A) nested with the first-generation regional model GoM-FVCOM (panel B). The blue line shown in panel B is the location of the nesting boundary; the blue line shown in panel A is the location of the nesting boundary between the UG-RCA water quality model and Mass Bay-FVCOM.
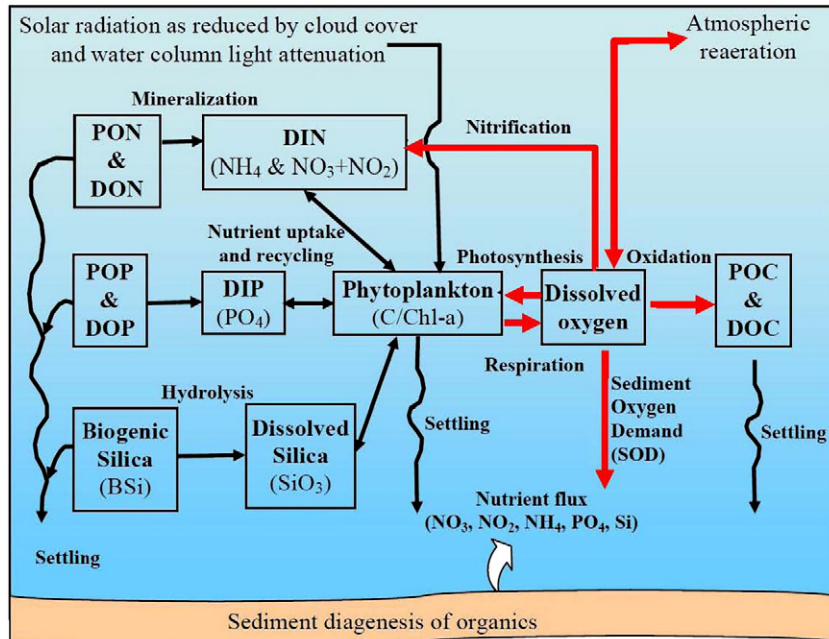

Fig. 4. The RCA water quality model structure.
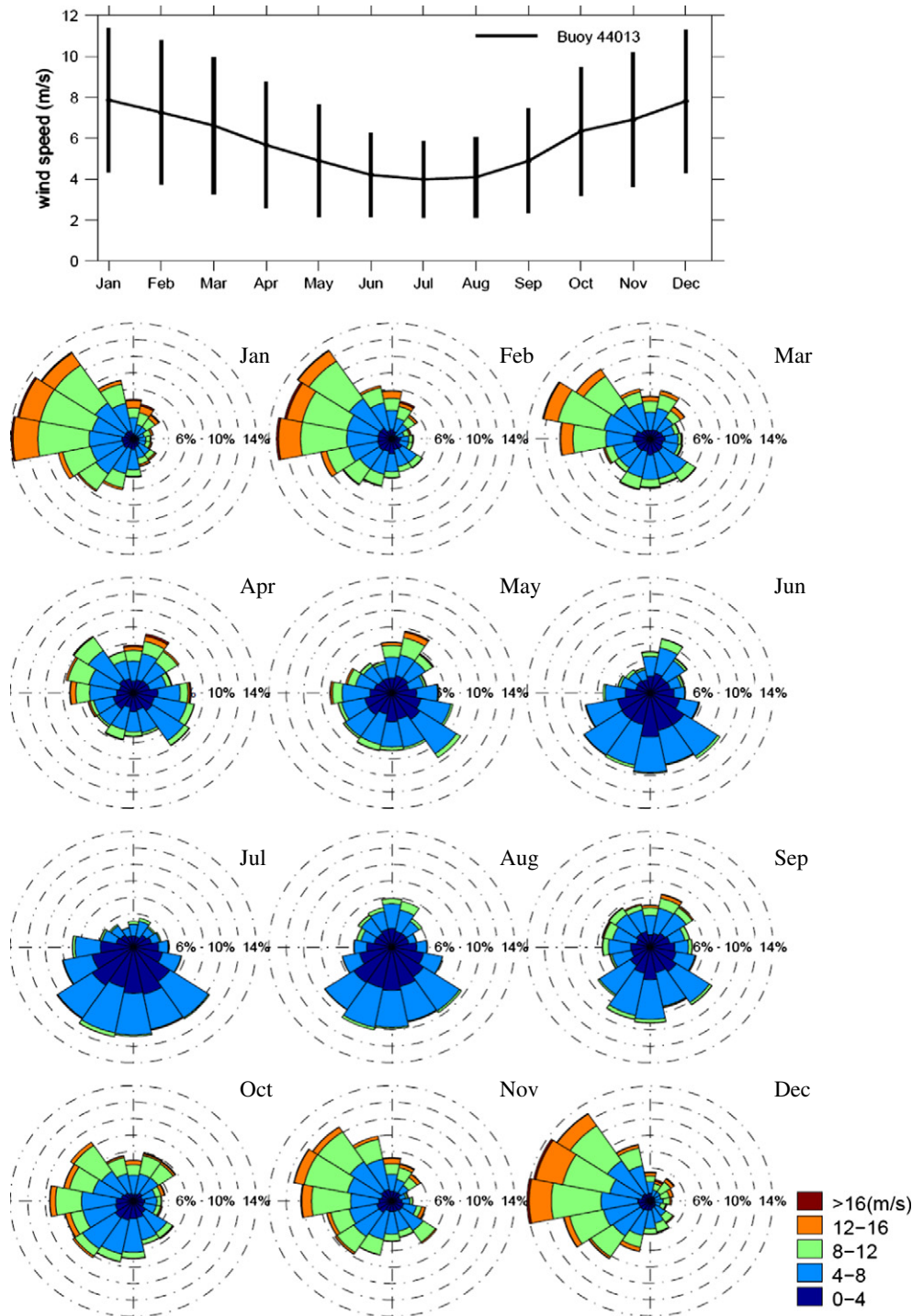Reproduced from HydroQual RCA 3.0 user guide, 2004.

Fig. 5. Upper panel: monthly-averaged wind speeds at NOAA buoy 44013 (42.346°N, 70.651°W) derived from hourly wind data from the National Buoy Data Center for the period 1995–2008. Vertical lines denote the standard deviation of wind speed from its mean value. Lower panel: wind rose plots based on the same dataset. The length of each "spoke" around the circle represents the frequency of time (%) that the wind blows from that direction. Each concentric circle represents a different frequency, emanating from zero at the center to increasing frequencies at the outer circles. All wind roses use 16 cardinal directions (e.g. north (N), NNE, NE, etc.). Wind speeds are presented in 4 m s^{-1} bins using the color bar in the lower right.

the physical and water quality models. We refer interested readers to Chen et al. (2010), Tian et al. (2010) and Zhao et al. (2011) for details of UG-RCA model development and validation.

A schematic of the RCA water quality model is shown in Fig. 4 (HydroQual, Inc., 2004). Biogeochemical variables include three phytoplankton assemblages (spring, summer and fall groups), four nutrients (ammonia, nitrate/nitrite, phosphate and dissolved silica), four organic phosphorus forms, four organic nitrogen pools, six organic carbon pools (four labile and refractory dissolved and particulate forms plus the reactive and exudates components), biogenic silica, and dissolved and aqueous oxygen. In the model, DO is computed by the surface flux through reaeration, bottom flux through sediment oxygen demand (SOD) and processes of oxidation of organic matter, nitrification and photosynthesis-respiration of phytoplankton within the water column. The growth of phytoplankton is controlled by the light intensity, temperature and uptake of dissolved inorganic nutrients including
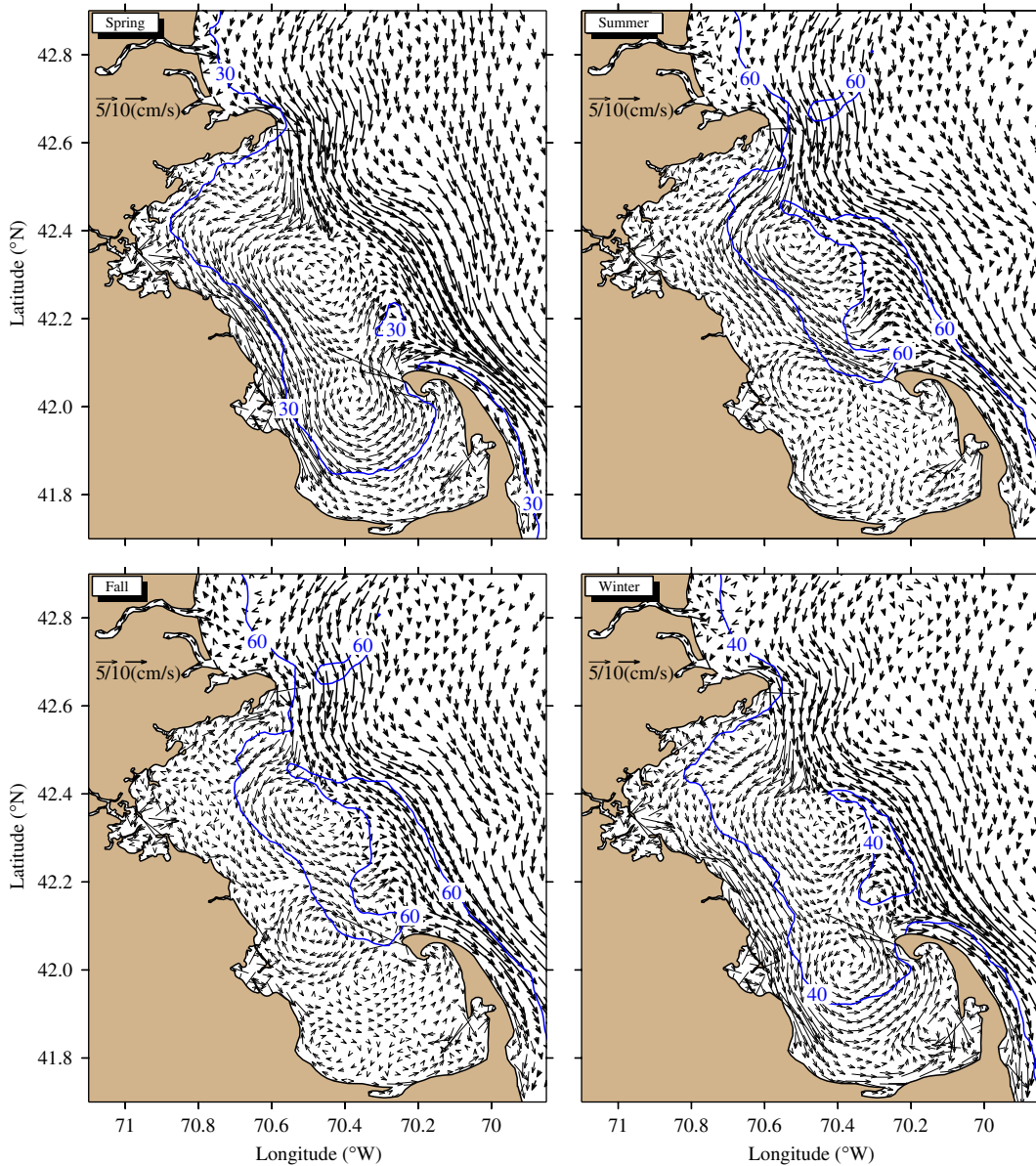
Fig. 6. Distributions of model-computed vertically-averaged seasonal mean current in MB over the period 1995–2010. Upper left panel: spring (March–May); upper right panel: summer (June–August); lower left panel: fall (September–November); lower right panel: winter (December–February). Blue line: local isobaths that circulation follows. Notice the current velocities outside Mass Bay were plotted (bold black arrows) at 50% scale of the velocities inside Mass Bay (black arrows).

ammonium NH_4^+, nitrate NO_3^- and nitrite NO_2^-, phosphate PO_4^{3-} and dissolved silica (e.g. $Si(OH)_4$). The loss of phytoplankton is transformed into organic matter through "grazing", mortality and exudation. The nutrient regeneration is produced by either remineralization of organic matter into inorganic nutrients in the water column or diagenesis processes in which organic matter settle down into sediment being transformed into inorganic nutrients and re-enter the water column through the sediment–water interface. The formulations used to describe DO-related biogeochemical processes in RCA are detailed in Appendix B, and further discussed in Section 5.

UG-RCA is driven by Mass Bay-FVCOM and atmospheric surface forcing (winds and solar irradiance). Nutrients and carbon loadings from point sources (e.g. the sewage outfall), non-point sources (e.g. groundwater), rivers and atmosphere are the major anthropogenic perturbations to the system, which are specified by measurement data. The initial and boundary conditions are specified using in situ data recorded at the monitoring sites or on routine surveys. Biogeochemical open boundary conditions were specified for 14 measured parameters:

chlorophyll-a, DO, NH4+, $NO^{2-} + NO^{3-}$, PO4^{3-}, Si(OH)^4, DON, DOC, DOP, PON, POC, POP, and biogenic silica, which are determined using an objective analysis (OA) of the bi-monthly field measurement data, developed by Hendry and He (1996). In the OA procedure, the covariance function between data and estimation site is based on their decorrelation scales: 30 km in the horizontal, 15 m in the vertical, and 45 days in time. Given limited sampling stations, it was the best approach available at the start of this study for water quality model boundary condition setup (Chen et al., 2010; Jiang and Zhou, 2004; Tian et al., 2009).

2.2. Observational data

A monitoring program for water quality in Mass Bay, supported by the Massachusetts Water Resources Authority (MWRA), was launched in 1992 and has been continued to present. The field measurements were made with monthly/bimonthly frequencies at so-called "near-field" and "far-field" stations, respectively (Fig. 1). Taking the location

of the sewage outfall as a reference point, the "near-field" stations refer to the measurement sites (with a total of 7) within 7 km relative to the sewage outfall, while the other sites are defined as "far-field" stations (with a total of 27). Monitoring variables include water temperature, salinity, DO, nutrients, chlorophyll-a, plankton, fish chemistry and pathology, sediment contaminants, etc. (Libby et al., 2003, 2004, 2007; Maciolek et al., 2009; Tucker et al., 2008). Water samples were collected at five standard levels at sites with water depth ≥ 15 m and three standard levels at shallower sites. More details of this monitoring program are available at http://www.mwra.state.ma.us/harbor/enquad/trlist.html.

2.3. Design of experiments

The primary objective of this study is to describe the temporal and spatial variation patterns of DO and examine the physical and biogeochemical processes that regulate such variability. To achieve this goal, we first analyzed the long-term monitoring data to characterize the temporal variability of DO in Mass Bay (see Fig. 2 for summary of findings). The monitoring data, however, were collected with low frequency in time and sparse resolution in space, so that they are not sufficient to resolve the spatial variation pattern in the entire bay. We then applied the Mass Bay-FVCOM/UG-RCA model to simulate the fields of DO and other key water quality variables over the period 1995–2010, during which the Mass Bay-FVCOM physical fields and the major monitoring program data were available. The model results were validated using all available observational data at the time and locations where the measurements were made. EOF analysis was then used to characterize the dominant temporal and spatial modes in the validated model fields. To help identify the key physical and biogeochemical processes controlling the observed and modeled DO variability in Mass Bay, four process-oriented experiments were conducted with UG-RCA.

3. Observed and simulation results

3.1. Observed and model-computed physical fields

The 1995–2010 monthly-averaged fields of winds over Mass Bay showed a clear seasonal cycle. This cycle, for example, can be seen in wind data collected at the Boston entrance NOAA buoy 44013 station (42.346°N, 70.651°W), located 26 km east of Boston. The mean wind speed was ~8 m s^{-1} in winter and ~4.5 m s^{-1} in summer, with an interannual variability of 3–4 m s^{-1} and ~2 m s^{-1}, respectively (Fig. 5). Here the interannual variability was estimated as one standard deviation (std) relative to the monthly mean. In this region, the downwelling-favorable winds from the northwest prevailed in winter and the upwelling-favorable winds from the southeast in summer, with transitions in spring and fall seasons. The maximum wind velocity can reach >16 m s^{-1}, which frequently occurred during episodic nor'easter storm events.

Correspondingly, the vertically-averaged subtidal currents in Mass Bay were characterized by the wind-driven and river discharge-induced buoyancy flow plus the southward extension of the WMCC. The model-computed flow (Fig. 6) was consistent with the conceptual circulation patterns shown in Fig. 1, which were based on previous measurements by Geyer et al. (1992). With a high-resolution grid and better geometric fitting, Mass Bay-FVCOM provided much finer temporal and spatial structures of the circulation in this coastal region. During spring, the flow in Mass Bay was controlled dominantly by the inflow of the combined Merrimack River plume, WMCC, and downwelling-favorable winds. The water entering MB flowed along local isobaths towards CCB at a speed of ~5 cm s^{-1}. After entering CCB, it turned cyclonically following the ~30-m isobath, with a main branch flowing out of the bay around the northeastern tip of Cape Cod and a weaker branch forming a cyclonic eddy in the eastern side of CCB. During

summer, driven by the southerly wind, the major southeastward flow was more likely along the ~60-m isobath out of MB towards the tip of CCB, and the flow in CCB was characterized with multiple weak mesoscale eddies. A similar flow pattern was also seen in autumn with current speed decreasing to a minimum of 1–2 cm s^{-1}. During winter, the currents strengthen again along the 30–40 m isobaths in the nearshore region, with this coastal flow moving southward into CCB and then rotating cyclonically like the recirculation pattern detected during spring. Seasonal patterns of the circulation in Mass Bay clearly showed that the water exchange between MB and CCB was more active in winter through spring but very weak in summer through autumn. This feature resulted in a relatively "isolated" ecosystem with a longer residence time in CCB during summer through autumn, so that the key mechanisms controlling the DO variation could significantly differ in the northern and southern regions of Mass Bay in these two seasons.

Water stratification and mixing in Mass Bay also exhibited clear spatial and temporal variability. In nearshore regions, as a result of wind and tidal mixing, waters remained vertically well mixed throughout the entire year, while in offshore regions, driven by seasonal heat flux variation, waters were strongly stratified during summer. The mixing depth can reach down to 80 m during the winter and be limited to the upper 10 m near surface during summer. The averaged water temperature over the entire model domain (Fig. 7, upper panel) indicated that well-mixed water occurs during November to March, while stratification starts in April and erodes during October. For example, the modeled water temperature at station F17 in the deep basin (Fig. 7, lower panel) reached the lowest value of <4 °C during March and the highest value of >18 °C in late August. The strongest stratification occurred in July–August, and when the water was vertically well mixed in October, the water column remained warm (with a temperature of >8 °C) until late November.
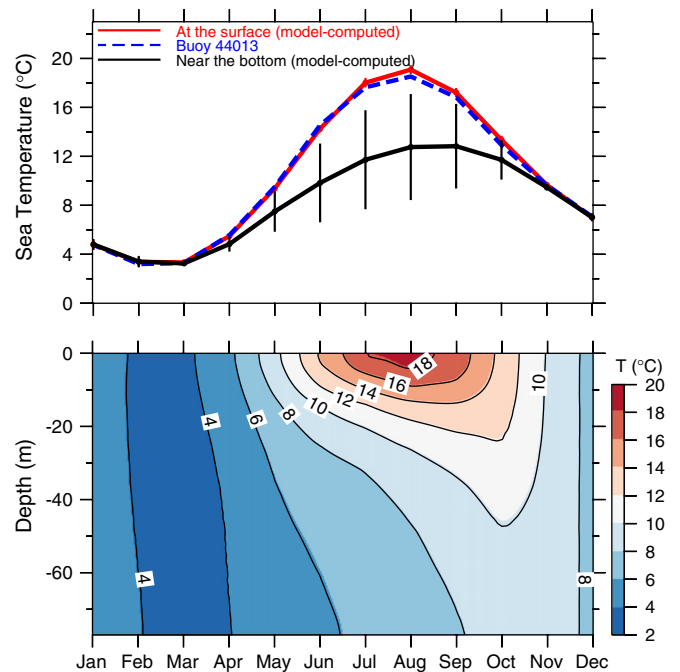

Fig. 7. Upper panel: comparison of observed and model-computed monthly-mean temperature. Blue dashed line: observed data at NOAA buoy 44013; red line: model-computed at the surface; black line: model-computed near the bottom. The vertical bars are the standard deviation. Lower panel: model-computed monthly-averaged temperature profile at station F17 (see Fig. 1 for location).
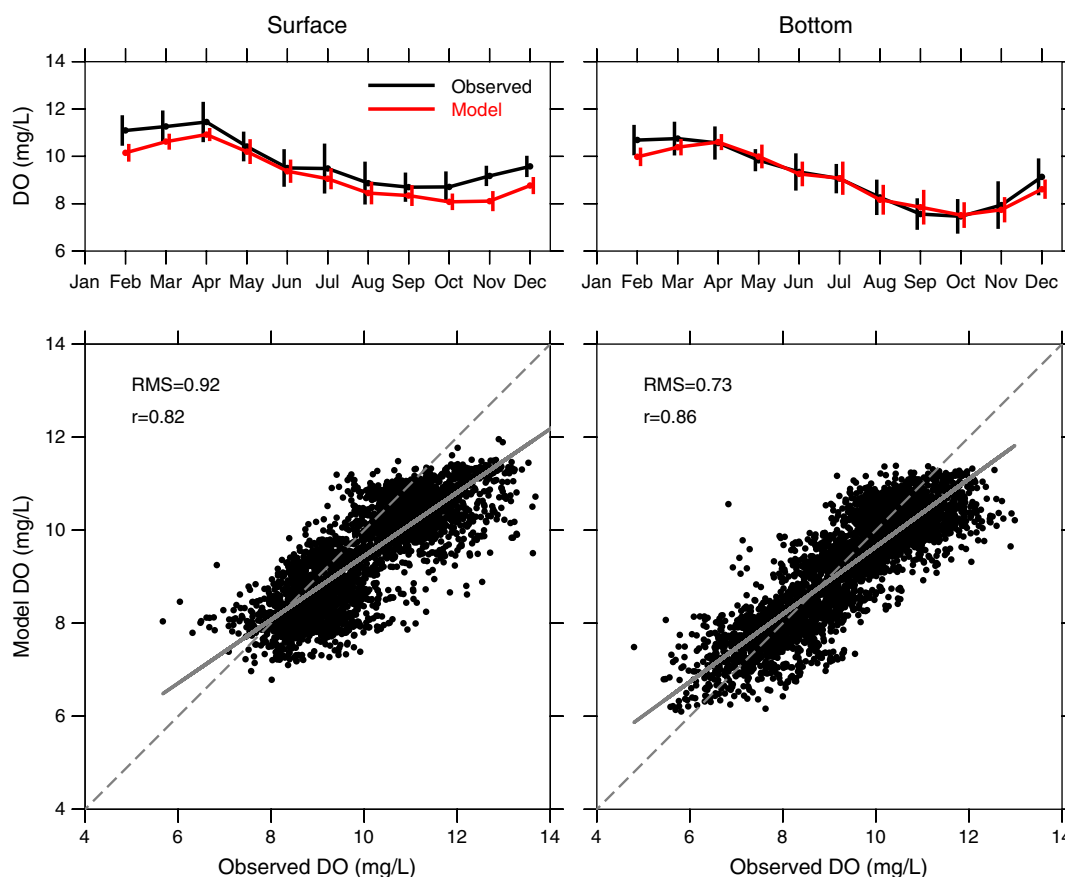
Fig. 8. Upper panel: comparison for model-computed (red) and observed (black) monthly-averaged DO concentration near the surface (left) and the bottom (right), respectively. Averaging was performed at all monitoring stations. The vertically oriented bars are the standard deviation relative to its mean value over 1995–2010. Lower panel: scatter plots of model-computed DO via observed DO at all stations in MB near the surface (left) and near the bottom (right) over the period 1995–2010. Solid lines indicate the best fit between model-computed and observed DO values. Dashed lines are a diagonal line representing a perfect match. Correlation coefficients (r) and RMS error between model-computed and observed values were estimated under p-value <0.05 (significance level).

3.2. Model-computed water quality fields

3.2.1. Dissolved oxygen

The model-computed monthly means of DO concentration over 1995–2010 were in good agreement with observations, not only in its value but also in its change over seasons (Fig. 8, upper panel). Both model results and observed data showed the highest DO concentration in April, gradually decreasing through May–September, and reaching its minimum in October. The DO concentration increased again afterwards in winter and this increase lasted until next March–April, forming the seasonal cycle. The correlation between modeled and observed DO concentrations was 0.82 near the surface and 0.86 near the bottom, with a root-mean square (RMS) error of ~0.92 and ~0.73 mg/l, respectively (Fig. 8, lower panel). Based on the two-sample t-test under the p-value <0.05 (significance level), the difference between modeled and observed DO concentrations near the bottom was not significant while the difference near the surface was statistically significant, with the modeled DO concentration slightly underestimating the observed, particularly during November through next February.

The model-computed DO concentration in Mass Bay was characterized by the spatial patterns shown in Fig. 9 (upper panel). From January to March, the DO concentrations were higher in the southern region (CCB) than in the northern region (MB), and along the coast than in the offshore deeper region, although its value was >9 mg/l over the entire Mass Bay. From May to September, the DO concentrations were higher in the northern region (MB) and lower in the southern region (CCB). The largest south–north DO gradient occurred in July. This distribution pattern was reversed again with higher DO in CCB and lower in MB in October and the revised pattern remained through winter. F02

and F17 are monitoring stations located in CCB and in MB, respectively. The comparison of DO concentrations at these two stations (Fig. 9, lower panel) illustrates that the DO concentrations in the southern region of Mass Bay showed a phase-leading to that in the northern region of Mass Bay, although they exhibited similar seasonal variability. For example, in March–April, the DO concentration was in the beginning of its decreasing phase in CCB (from 11 mg/l to 10.7 mg/l over a month, accounting for 8% of total DO variation), while it was still in the end of an increasing phase in MB (from 10.4 mg/l to 10.6 mg/l over a month, representing 6% of total DO variation). The DO concentrations in these two regions tended to converge to a similar value in April and then diverged afterward with an increase in the north–south DO gradient during summer. A similar case happened in October, during which the DO concentration started to turn into an increasing phase in CCB, while it still experienced a decreasing phase in MB.

3.2.2. Dissolved inorganic nitrogen

The model succeeded in simulating the dissolved inorganic nitrogen (DIN) concentration, not only in spatial distribution but also seasonal and interannual variations (Fig. 10, upper panel). The correlation between model-computed and observed DIN concentrations was 0.79 near the surface and 0.55 near the bottom. The monitoring data showed that DIN was replenished in the winter-mixing season, during which the DIN concentrations at the surface and bottom were nearly the same. This replenishment pattern was well captured by the model. The monitoring data also indicated that in surface waters, DIN concentrations started to decrease in March through April following spring phytoplankton blooms (Fig. 10, lower panel), and remained at a low level during summer through early fall as a result of strong stratification
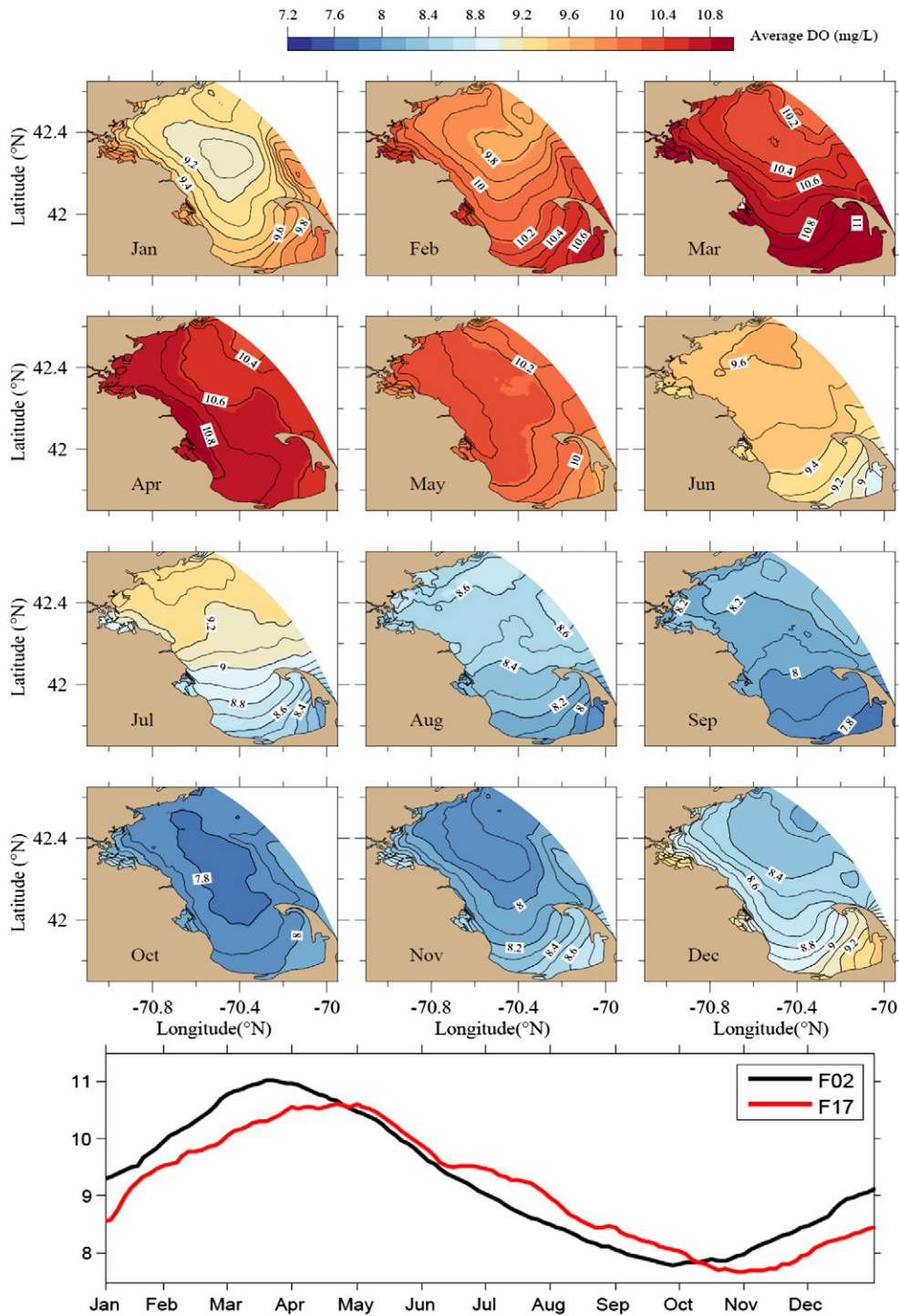
Fig. 9. Upper panels: distributions of model-computed vertically-averaged monthly-mean values of DO concentration in MB over the period 1995–2010. Lower panel: the time series of model-computed vertically-averaged monthly-mean values of DO concentration at station F02 (see Fig. 1 for location) in the southern bay and at station F17 in the northern bay.

(Fig. 7). The model also accurately reproduced this observed seasonal variability. Since the physical model successfully simulated vertical stratification and mixing, the water quality model was capable of resolving the observed large vertical gradient of DIN between the bottom and surface waters. This resulted from the restriction of vertical water exchange under the stratified condition. The model was also capable of reproducing the rapid increase of DIN near the surface from October through December as vertical mixing was strengthened (Fig. 7; Fig. 10, upper panel). Both model and observation showed that DIN exhibited

significant interannual variability within a range of ~2–8 μM. Large variation (5–6 μM) persists in all seasons near the bottom but was much reduced during summer near the surface. In Mass Bay, particularly in the stratified regions, the euphotic layer was about the same order of the surface mixed layer. DIN was limited to ≤2 μM near the surface during summer, but remained at a level of ~5 μM or more in the bottom layer beneath the seasonal thermocline in summer. The regeneration through local remineralization, input from the sediment to the water column, horizontal transport of nutrients and organic matter from
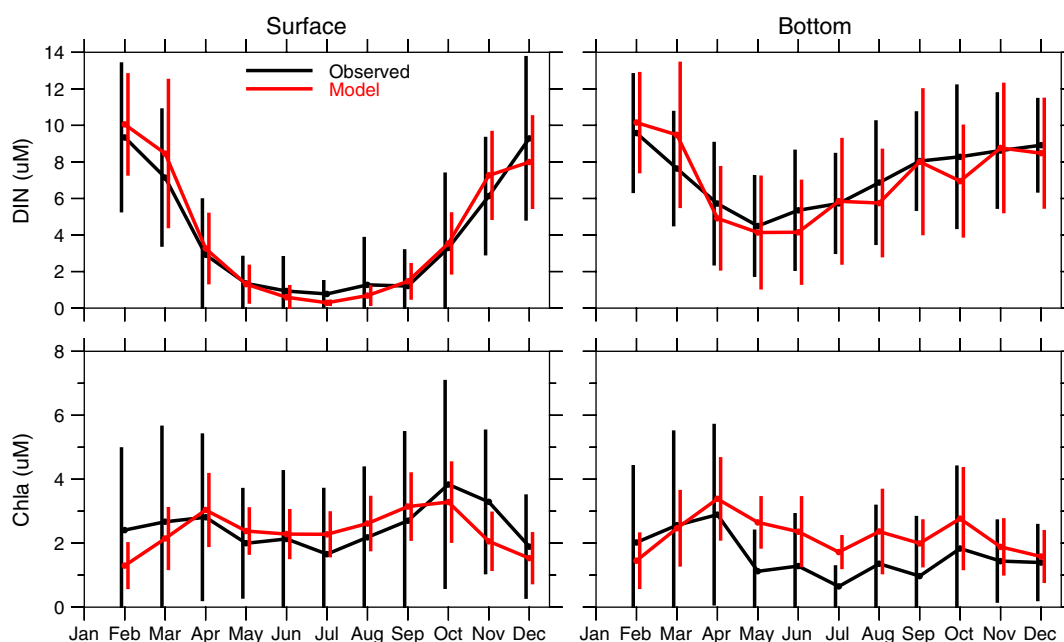
Fig. 10. Comparison for model-computed (red) and observed (black) monthly-mean values of dissolved inorganic nitrogen (upper panels) and chlorophyll-a (lower panels) near the surface (left) and the bottom (right). Vertically oriented lines indicate the standard deviations.

upstream, and wind- and cooling-induced vertical mixing were key processes to keep DIN concentration high throughout the water column during late fall through winter (Jiang et al., 2007).

3.2.3. Chlorophyll-a

The monitoring data showed that the phytoplankton biomass in Mass Bay was characterized by two seasonal blooms: the spring bloom in April and the fall bloom in October. Since the timing of these blooms varied significantly each year, the bloom signals were not significant in the monthly-mean values averaged over the 16-year study period, although they were still noticeable (Fig. 10, lower panel). Fig. 10 also shows that the interannual changes in chlorophyll-a (Chl-a) concentration were larger than its mean value. The model successfully captured both spring and fall blooms in individual year simulations, but was incapable of reproducing the large interannual variability detected in the observations. The model and observed 16-year mean Chl-a concentrations were 2.4 and 1.6 μg/l near the surface and 2.5 and 2.2 μg/l near the bottom, with a surface-bottom difference of only −0.1 μg/l for the model and −0.6 μg/l for the observations. The overall RMS errors between modeled and observed Chl-a concentrations at all stations were 2.42 μg/l near the surface and 2.15 μg/l near the bottom. One possible reason is that this water-quality model was developed without inclusion of harmful algae bloom (HAB) dynamics. HABs have become a more frequent spring or summer feature in Mass Bay (Anderson et al., 2005), which can cause a large short-term increase in near-surface Chl-a. In addition, while a major effort was made to carefully categorize the phytoplankton species into three phytoplankton assemblages (spring, summer and fall groups), the cellular composition of the Chl:C ratio was difficult to be represented accurately in the model due to the complexity of the phytoplankton species in this region.

4. Empirical orthogonal function (EOF) analyses

An empirical orthogonal function (EOF) analysis was performed to synthesize the temporal and spatial fluctuations in DO concentration in Mass Bay. Singular value decomposition was used to obtain the dominant EOF modes and principal components (Lagerloef and Bernstein, 1988; Preisendorfer, 1988). To focus on seasonal and interannual variability, the EOF analysis was done using monthly-averaged fields, with

no attempt to resolve higher frequency variability with time scales shorter than one month. A brief description of the EOF method used in this study is given in Appendix A.

The EOF analysis on the 16-year simulation DO fields produced two dominant modes that account for 98.6% of the total variance of DO concentration. The 1st EOF mode represents the seasonal cycle and accounted for 94.3% of the total variance (Fig. 11a). The amplitudes of this mode have the same sign (all positive) and were in a range of 1.4–1.7. Combined with the corresponding amplitude time series (Fig. 11c), we can see that the dominant variation in DO concentration over the entire Mass Bay was primarily characterized by seasonal variability, with the highest concentrations occurring in spring and lowest in fall, consistent with observations (Figs. 8, 9). This seasonal variability exhibited larger amplitude in the southern region (CCB) than in the northern region (MB) (Fig. 11a). The amplitude time series also exhibits significant interannual variations. For example, DO concentrations during the fall season were lower in 1999 than in other years, in agreement with monitoring data reported by Libby et al. (2007).

The 2nd EOF mode accounted for 4.3% of the total DO variance and had opposite signs in the northern (MB) and southern (CCB) regions (Fig. 11b). This suggests that there was a secondary spatial pattern with opposite phase in these two regions. The corresponding amplitude time series showed a phase-shift relative to the 1st EOF mode, with peaks appearing in winter and troughs in summer. In Fig. 9, both observations and model results at F02 and F17 indicate that the DO variation in CCB was leading to that in MB. This feature can be reproduced by a superposition of the 2nd mode on the 1st mode. Since these two modes implied different characteristics, this suggests that the DO variations in the southern and northern regions were driven by different dynamics. The process-oriented experiments described in the next section were aimed at addressing this question.

5. Physical and biogeochemical mechanisms for DO variations

5.1. Mechanisms controlling the DO seasonal variation in Mass Bay

The variability of DO concentration in Mass Bay was controlled by physical and biogeochemical processes. The physical processes include advection, vertical mixing and lateral diffusion, while the
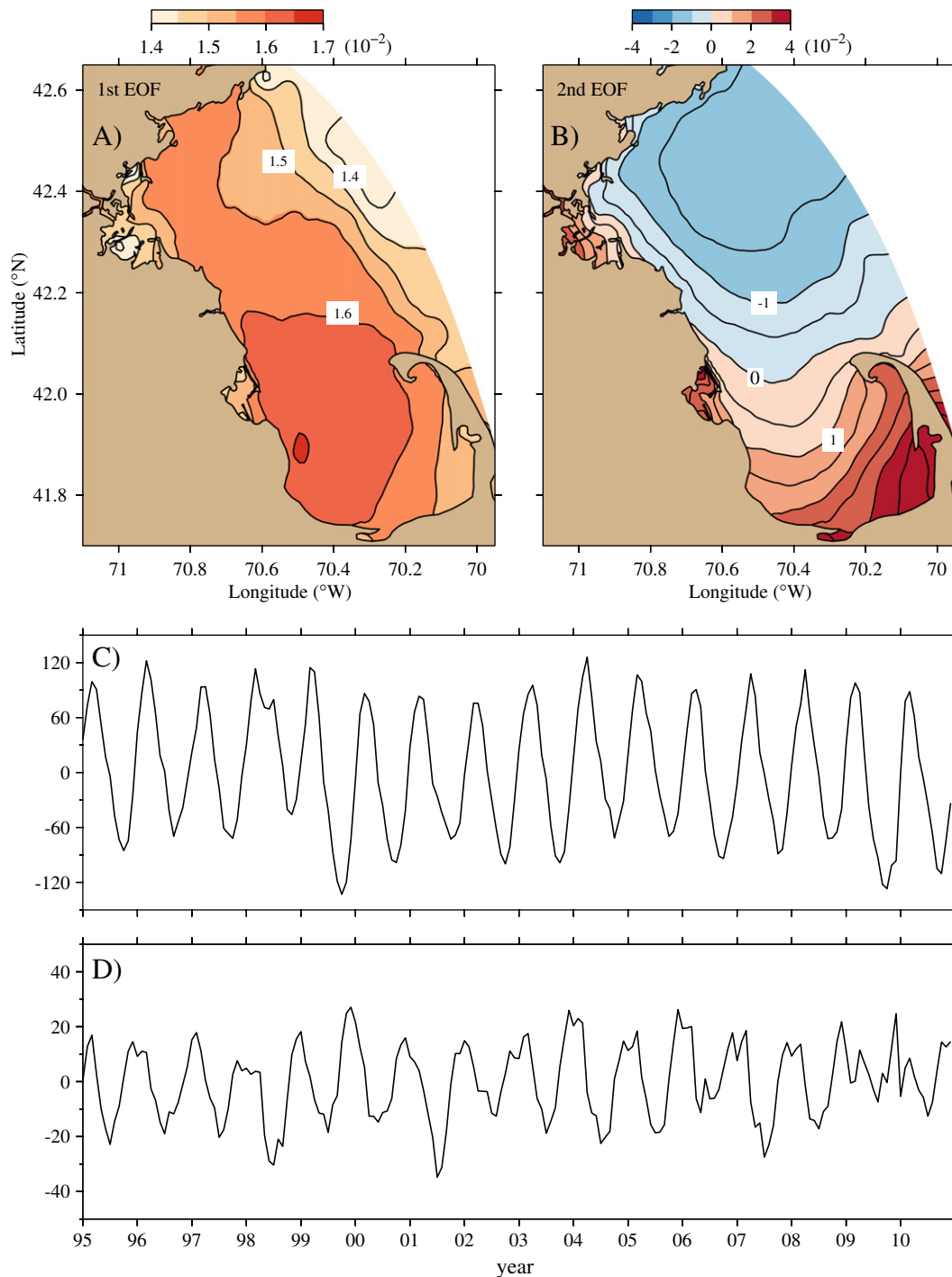
Fig. 11. Spatial distribution of DO concentration for the 1st (a) and 2nd (b) dominant EOF modes plus time series of the temporal amplitude associated with the 1st (c) and 2nd (d) EOF modes. The EOF analysis was done for model-computed monthly-mean DO concentration fields over 1995–2010.

biogeochemical processes are reaeration, photosynthetic production, minus phytoplankton respiration, oxidation of organic carbon, sediment oxygen demand (SOD), nitrification, and sulfide oxygen equivalents. Detailed empirical formulations of these biogeochemical functions are described in Appendix B. The fact that DO in Mass Bay exhibited relatively small interannual variability while nitrogen and Chl-a concentrations varied significantly over seasonal and annual time scales implies that biogeochemical factors offset each other to form a relatively stable net balance. Mass Bay water is supplied by inflow on the northern boundary connected to the western Gulf of Maine shelf (Fig. 6). The cyclonic circulation in Mass Bay is a key advection process to transport DO from the northern region (MB) to the southern region (CCB). Since the intensity

and spatial scale of this circulation pattern varied significantly seasonally and CCB featured a multi-meso-scale eddy field in summer and fall, the role of advection could significantly differ in MB and CCB.

In order to examine the roles of advective and local biogeochemical processes in DO variation in Mass Bay, we performed four diagnostic experiments to identify and qualify relative contributions of these processes. Since the interannual variation of DO was small, we selected one year (2008) as representative and ran UG-RCA model by turning off: *a*) the air–sea oxygen exchange process (Ex#1); *b*) the oxygen production and consumption through photosynthesis minus respiration, organic matter oxidation and nitrification (Ex#2); *c*) the SOD (Ex#3); and *d*) all biogeochemical processes (Ex#4). A comparison of monthly-
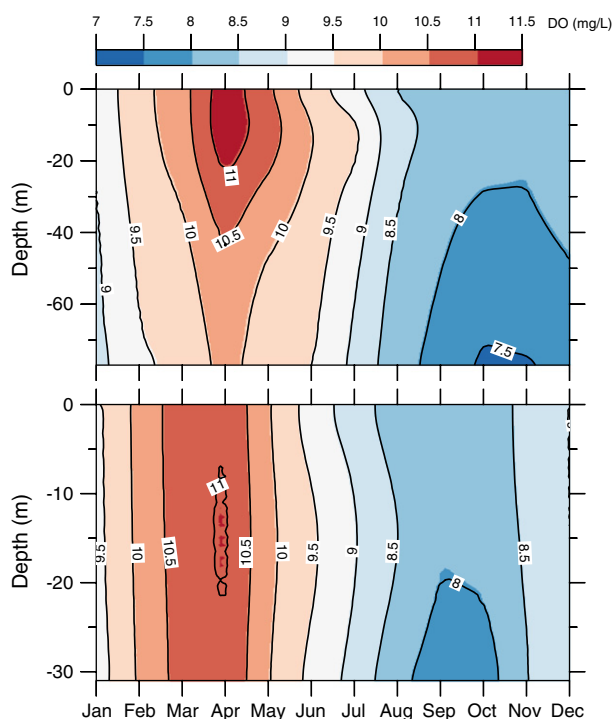
Fig. 12. Model-computed monthly-mean values of DO profiles at station F17 (upper panel) in the northern bay and station F02 (lower panel) in the southern bay for 2008.

mean DO profiles for these four experiments was made at station F17 in MB and station F02 in CCB.

Compared to the standard run of 2008 (Fig. 12, upper panel), all four experiments at station F17 produced similar seasonal patterns of DO concentration: highest DO near the surface during spring and lowest near the bottom during autumn (Fig. 13). In Ex#1, removing reaeration caused higher DO concentrations in the upper mixed layer near the surface in summer and lower throughout the water column in winter. As described in Eq. (B-2) in Appendix B, the reaeration depended on the DO saturation concentration (Fig. 14). During summer, due to high water temperatures, the DO saturation concentration was lower than the actual DO concentration at the surface (Eqs. (B-2), (B-4), Appendix B). Thus, the water was *oversaturated*, and the air–sea oxygen exchange transferred DO from the water to the air. Since the water was strongly vertically stratified, this process mainly affected the DO concentration near the surface. During winter, however, due to surface cooling, the DO saturation concentration was higher than the actual DO concentration at the surface. Therefore, the water was *undersaturated*, and the water gained DO from the air (Eq. (B-2), Appendix B). Since the water was vertically well mixed, this process had an impact on DO throughout the water column. The overall contribution of reaeration to the DO concentration was relatively small. The maximum difference was only 0.575 mg/l, which accounted for ~5.0% and ~0.6–0.7% of the total DO concentration during summer and winter, respectively.

In Ex#2, removing the oxygen production through photosynthesis minus respiration (Eqs. (B-5), (B-20), Appendix B), organic matter oxidation (Eq. (B-21), Appendix B) and nitrification (Eq. (B-22), Appendix B) mainly caused a difference in the upper layer during spring (~−0.5 mg/l) and summer (~−0.25 mg/l) and in the deep layer during fall and winter seasons (~0.13 mg/l). As in Ext#1, the contribution of these biogeochemical processes to the total DO concentration was only about 2.0–4.0% during spring through summer and about 1.5% during fall through winter. In Ex#3, removing the SOD (Eq. (B-24)) caused only a small difference near the bottom, with its maximum of ~0.13 mg/l. This process was negligible for the DO seasonal variation.

In Ex#4, keeping only the physical processes was capable of producing the same seasonal pattern of DO concentration at station F17. The difference shown there was caused by the combined contribution of the biogeochemical processes. This difference, however, only accounted for ~3.0–4.0% of the total DO concentration. Although this difference was about 12% of the total DO seasonal variation range, it did not change the seasonal variation structure found in the observations and full UG-RCA model simulations. This result clearly demonstrated that the seasonal variation of DO concentration in the northern region (MB) was controlled primarily by horizontal advection plus mixing. Our finding here using the UG-RCA model is consistent with the statistical DO regression of Geyer et al. (2002), who found that DO variation in MB was highly correlated to that in the adjacent western Gulf of Maine shelf, and inferred that the variation of DO concentration in MB was controlled by the upstream inflow.

At station F02, the model-computed DO concentration was vertically well mixed in all seasons, with a difference of ~2.0 mg/l from January to July (Fig. 12, lower panel). Diagnostic analysis results suggested that the relative contributions of physical and biogeochemical processes to the DO seasonal variation in this region (CCB) were more complex than those found in MB (Fig. 15). In Ex#1, removing reaeration led to a difference of ~1–1.5 mg/l throughout the whole year (except in April and October during which time the DO concentration was close to its saturation concentration). This value was about 2–3 times larger than that at station F17 in MB, and accounted for up to 30–50% of the total DO seasonal variation range. As a result, the timing of the DO concentration peak was shifted from March–April to April–May. Similarly, the timing of the lowest DO was shifted from September–October to December.

In Ex#2, the maximum difference by removing oxygen production through autotrophic and heterotrophic processes was ~−0.5 mg/l, occurring in March–April. Without the contribution of photosynthetic production during spring and fall bloom seasons, the peak of the DO concentration value (which had a value of 11 mg/l) vanished in late March and early April. In Ex#3, due to the shallower depth and energetic vertical mixing in CCB, the influence of SOD was more significant in this region than in MB. The DO profile remained slightly changed before summer but the difference was up to ~0.5 mg/l in later summer and early fall seasons. Since vertical mixing was relatively strong during these seasons, the influence of SOD was throughout the whole water column and the DO profile was vertically uniform.

In Ex#4, removing all biogeochemical processes caused a time shift of the DO peak from late March to May (Fig. 15). The combined contribution of biogeochemical processes was ~−1.0 mg/l during winter through spring and ~1.0 mg/l in summer through early fall. Since the water in CCB was mostly from MB and the DO peak there occurred in April (Fig. 12), Ex#4 suggests that the advection time scale from the upstream northern boundary to CCB was about one month, which is about the same as the residence time estimated in the observing system simulation experiments in Mass Bay (Xue et al., 2012). The observed and model-simulated DO variation in CCB has showed a phase-leading to that in MB (Figs. 9 and 11). Comparing the results of Ex#4 with the standard run of 2008 clearly show that this phase-leading was caused by local biogeochemical processes. This was also demonstrated by the no biogeochemical process experiment in Ex#4, which showed a phase-delay (rather than a phase-leading) of DO variation in CCB to that in MB. This finding is consistent with the dynamical difference between southern and northern bays. Slow-moving eddy features in CCB produced a longer residence time thus allowing local biogeochemical processes to outweigh the advective and mixing processes.

5.2. Balance of biogeochemical processes in CCB

The DO variation is controlled by the total net flux that equals the sum of fluxes from individual physical and biogeochemical processes. Fig. 16 shows the vertically-averaged values of these fluxes with respect to the time of month at station F02 in CCB. This figure indicates that the
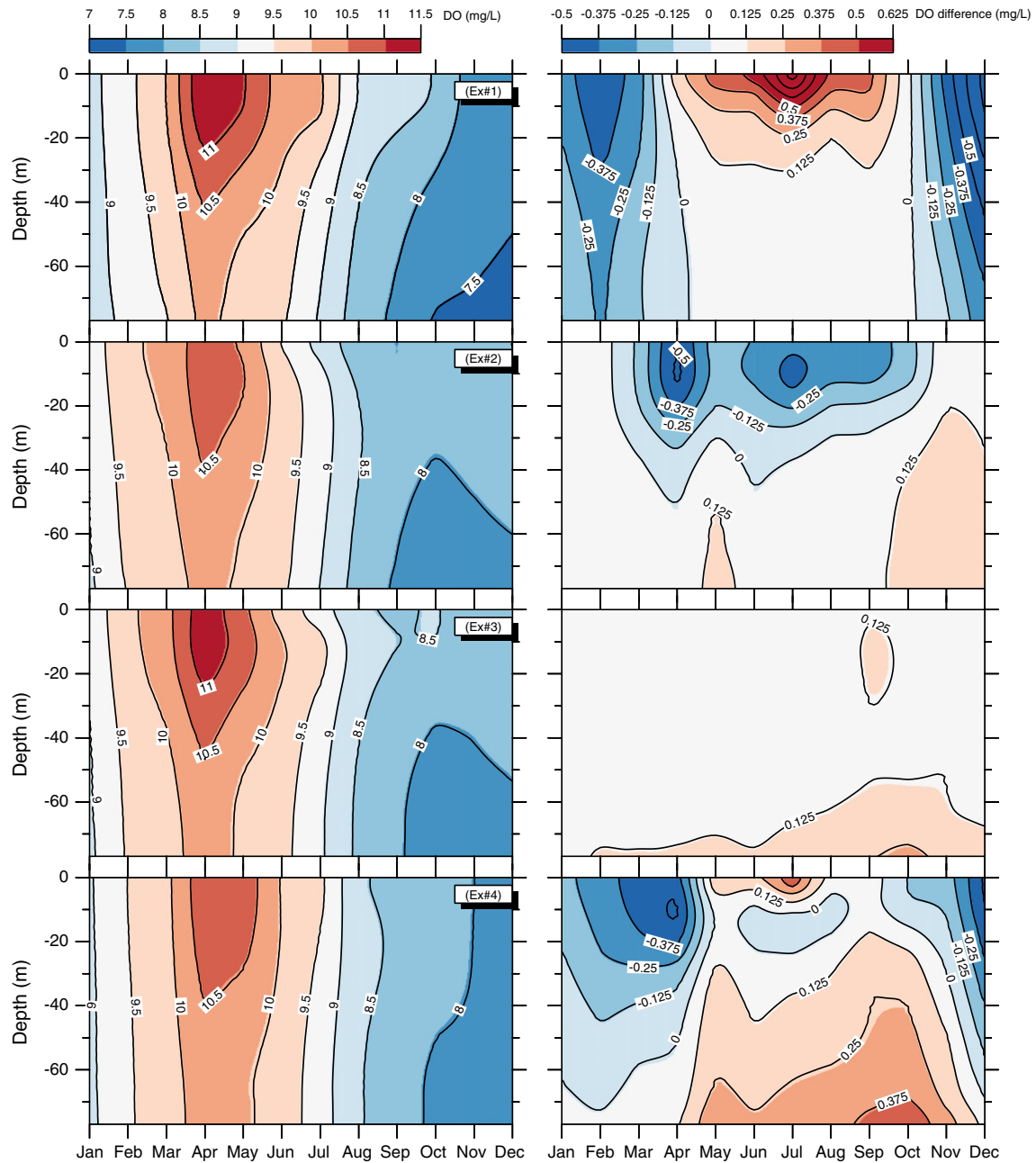
Fig. 13. Model-computed monthly-mean values of DO profiles (left) and their difference to the standard simulation results (with inclusion of all physical and biogeochemical processes) at station F17 for 2008 in the northern bay for Ex#1, Ex#2, Ex#3 and Ex#4, respectively.

variation of total net DO flux was dominated by reaeration during winter (November–January), during which reaeration accounted for a vertically-averaged DO increase of ~0.03–0.05 mg/l per day throughout the whole water column. Both the strong winds and low temperatures resulted in a strong reaeration process during the winter (Eqs. (B-3), (B-4), Appendix B). Reaeration plus vertical mixing was the key mechanisms to replenish DO annually from its losses in summer through fall. Other biogeochemical processes were offset to each other during most of the time over the year. For example, the photosynthetic production of DO produced the largest portion of positive DO flux during early spring and from late summer to early fall. This positive flux, however, was always accompanied by the negative DO flux generated through oxidation of organic matter, particularly during the fall season. Such a negative correlation between DO production and consumption persisted every

year, with a correlation coefficient of 0.77 (Fig. 17). Higher (lower) photosynthesis production (Eq. (B-5), Appendix B) led to higher (lower) oxidation-induced oxygen consumption (Eq. (B-21), Appendix B), when algal carbon inside phytoplankton was redistributed into organic carbon pool through oxidation via respiration and grazing. The net flux of these two biogeochemical processes was usually small compared with reaeration.

The phase-leading feature of DO variation in CCB could also be explained by reaeration variation in CCB and the northern bay. Since CCB was generally much shallower than the northern bay, the water temperature in CCB varied at a faster rate due to smaller water volume and thus causes a faster change in the DO saturation state (between undersaturated in winter and oversaturated in summer) in CCB than in MB, therefore the DO concentration modified by the change in the
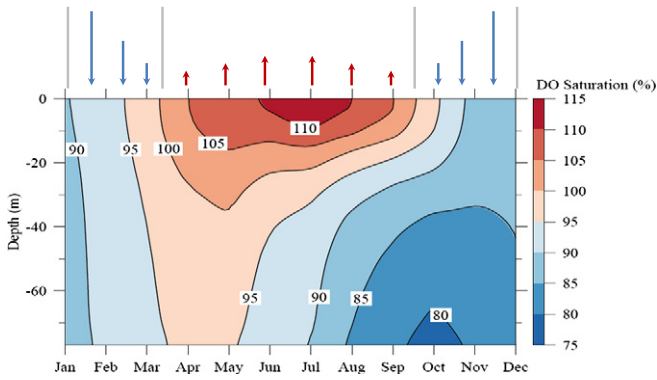
Fig. 14. Model-computed DO saturation percentage profiles at station F17 for 2008. The blue and red arrows indicate the direction of air–sea flux produced by reaeration.

direction of the DO flux through reaeration occurred earlier in CCB. This resulted in the phase-leading of DO variation in CCB. Meanwhile, the smaller water volume of CCB also allowed DO to reach a full equilibration with the atmosphere at a faster rate, which also contributed to the phase-leading of DO variation in CCB, particularly during the winter when the water was vertically well-mixed in the entire Mass Bay.

6. Conclusions

FVCOM/UG-RCA, a multi-domain-nested coupled physical and biogeochemical model, was used to simulate the water quality fields in Mass Bay for the period 1995–2010. Based on good agreement between model-computed and observed DO and nitrogen fields, an EOF analysis was conducted to characterize the dominant modes controlling the temporal and spatial variability of DO. Process-oriented numerical experiments were also made to identify and qualify the relative importance of physical and biogeochemical processes to the seasonal variation of DO in the northern (MB) and southern (CCB) regions.

The EOF analysis shows that the variability of DO in Mass Bay was dominated by two modes that accounted for 98.6% of the total variance in DO concentration. The 1st mode represents a well-defined seasonal cycle, with highest DO in March–April and lowest in October. The 2nd mode features a secondary spatial variation pattern with opposite phase between MB and CCB. Both observations and model results indicate that the DO peak occurs earlier in CCB than in MB. This feature can be reproduced with a combination of the 1st and 2nd modes.

The process-oriented experiments suggest that the seasonal variation of DO concentration was controlled primarily by horizontal advection plus mixing in MB and by local biogeochemical processes in CCB. Results have shown that resolving only physical processes can maintain to a large degree the temporal structure of DO variation in MB, but will cause a phase shift of temporal variation of DO in CCB. This feature is consistent with the dynamical difference between these two regions. Frequent appearance of mesoscale eddies in CCB produced a longer residence time favoring local biogeochemical processes to outweigh advection. In CCB, the variation of total net DO flux was dominated by reaeration during winter (November–January). Reaeration plus vertical mixing was the key mechanism to replenish DO annually from its losses in summer through fall, while other biogeochemical processes offset each other during most of the time over a year.

The important result of this work is to identify and quantify the complex multi-scale physical–biogeochemical interactions governing DO in Mass Bay and provide valuable information for optimizing the regional water quality monitoring network. Different mechanisms of DO

variation between MB and CCB suggest different strategies for the monitoring network design in Mass Bay for water quality forecasting: sampling stations near the north inflow passage are important for monitoring and forecasting water quality in MB, while sampling stations in CCB should be designed to capture the local biogeochemical processes.

Appendix A. EOF analysis method

In this study, EOF analysis was conducted by using monthly-averaged DO simulation results over a 16-year period. The total number of DO simulation fields (snapshots) (labeled N) was 192, and the total grid points in the computational domain (labeled M) were 5752. $D(x,t)$ is defined as a DO matrix of size M × N, where x and t represent the space and time coordinates. The residual matrix D' was then defined as

$$D'(x,t) = D(x,t) - \frac{1}{N}\sum_{i=1}^{N} D(x,t_i).$$

With standard singular vector decomposition (SVD), $D'(x,t)$ can be represented by

$$D'(x,t) \approx \sum_{i=1}^{m} \alpha_i(t) F_i(x)$$

where F_i is the ith spatial EOF mode (or principle component) and α_i is the temporal amplitude coefficient of the ith spatial mode. m is the total number of dominant modes, which is usually much smaller than the number of sampled fields N (this is the so-called low-dimension representation). α_i and F_i were calculated by minimizing the error $\varepsilon = D'(x,t) - \sum_{i=1}^{m} a_i(t)F_i(x)$ under the condition that the ith EOF mode is chosen to be orthogonal to 1st-$(i$-$1)$th EOF modes. These spatial patterns (EOF modes) are built to account for most of the system variance with the least number of orthogonal modes.

Appendix B. Biogeochemical formulations of dissolved oxygen

Dissolved oxygen (DO) concentration is a common indicator of the health of the aquatic ecosystem. DO simulation was made relating to a number of sinks and sources of DO processes involving the nitrogen cycle and phytoplankton. The sources of DO include re-aeration from the atmosphere (F_{reareo}) and photosynthetic oxygen production from aquatic plants ($F_{NH_4}^P, F_{NO_3}^P$). The sinks of DO include respiration by aquatic plants (F_{resp}), oxidation of carbonaceous and nitrogenous materials (F_{oxid}), nitrification (F_{nit}), sediment oxygen demand (SOD) (F_{SOD}), and sulfide oxygen equivalents ($F_{sulfide}$). A sum of these sources and sinks yields

$$DO = F_{reareo} + F_{NH_4}^P + F_{NO_3}^P - F_{resp} - F_{oxid} - F_{nit} - F_{sulfide} - F_{SOD}. \quad (B-1)$$
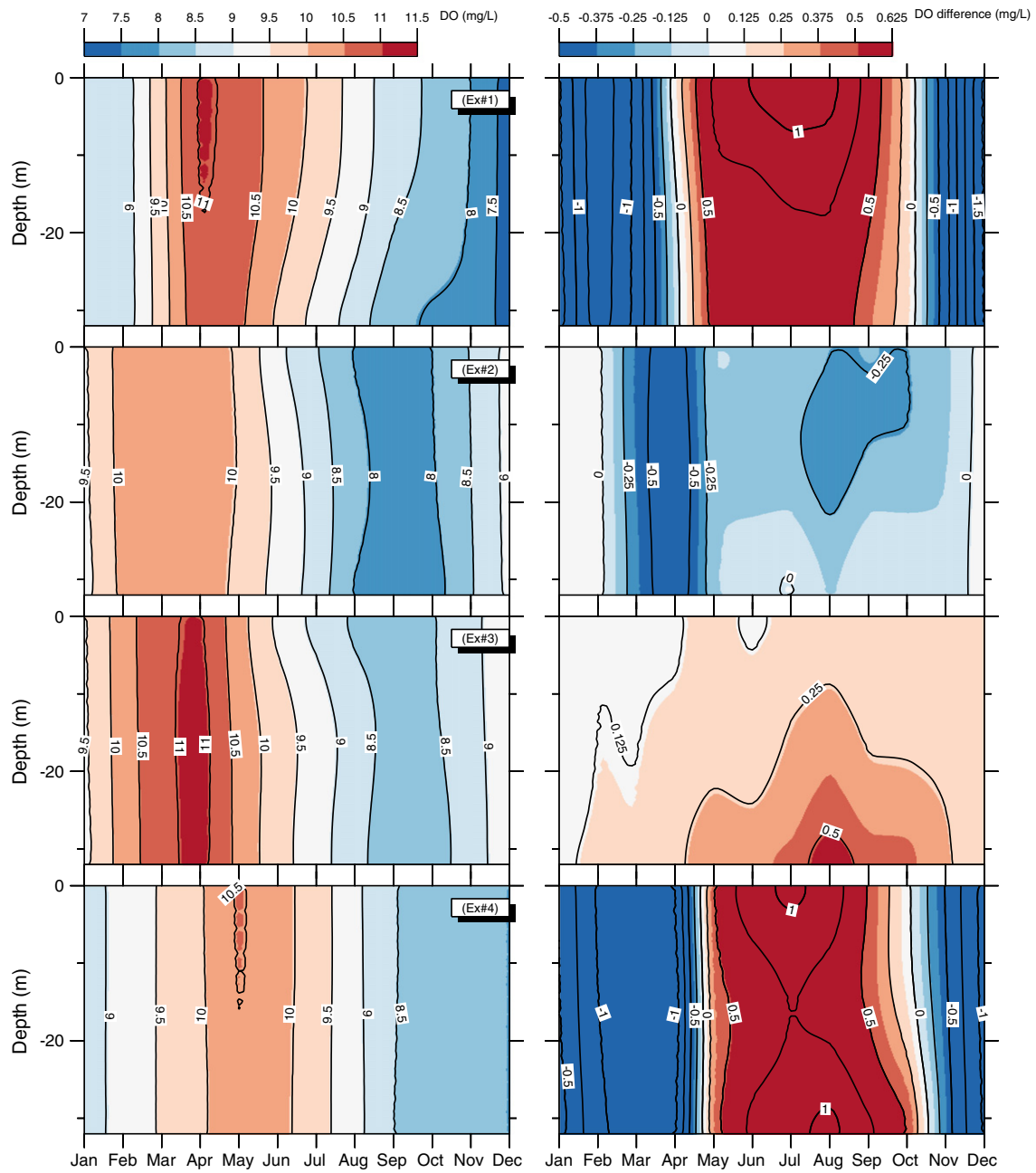
Fig. 15. Model-computed monthly-mean values of DO profiles (left) and their difference to the standard simulation results (with inclusion of all physical and biogeochemical processes) at station F02 in CCB for Ex#1, Ex#2, Ex#3 and Ex#4, respectively.

The formulations used to calculate each term in Eq. (B-1) are briefly described here and the definition, notation and value of parameters (denoted by a symbol "=") related to these formulations were listed in Table 2.(See Table 1.)

Reaeration F_{reareo} is calculated in the form of:

$$F_{reareo} = \frac{K_1}{H} \bar{\bar{\theta}}_a^{(T-20)} (DO_{sat} - DO) \qquad (B-2)$$

where $\bar{\bar{\theta}}_\alpha$ is the coefficient of temperature correction for reaeration, H is the layer depth and K_1 is the piston coefficient of oxygen air–sea exchange. K_1 is determined by wind speed (W_{wind}) using the formula given as

$$K_1 = 0.728\sqrt{W_{wind}} - 0.317W_{wind} + 0.0372W_{wind}^2. \qquad (B-3)$$
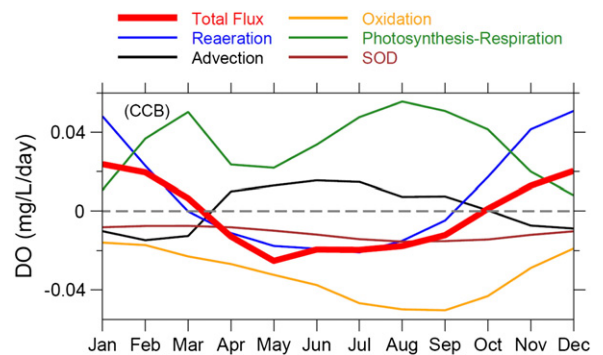
Fig. 16. Model-computed vertically-averaged monthly-mean values of DO fluxes in CCB for 2008. Dashed gray line indicates the line with zero flux.
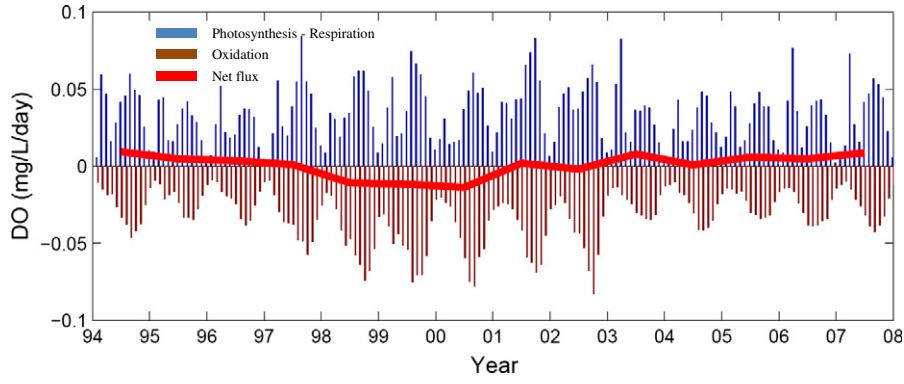
Fig. 17. Time series of model-computed vertically-averaged monthly-mean values of positive DO flux produced by photosynthesis-respiration production (blue bar) and negative DO flux caused by oxidation of organic matters (brown bar) as well as annual net flux (red line) in CCB over 1995–2010.

DO_{sat} is the DO saturation concentration, which is a function of water temperature (T) and salinity (S) given as

$$DO_{sat} = \exp[-139.34411 + 1.575701e^5/T - 6.642308e^7/T^2 + 1.243800e^{10}/T^3 \\ - 8.621949e^{11}/T^4 - S(1.7674e^{-2} - 10.754/T + 2140.7/T^2)]. \tag{B-4}$$

Photosynthetic production of DO $\left(F^P_{NH_4} + F^P_{NO_3}\right)$ is calculated by

$$F^P_{NH_4} + F^P_{NO_3} = \left[\overline{\overline{\alpha}}_{oc}\alpha_{NH_4} + a_{NO_{3c}}\left(1 - \alpha_{NH_4}\right)\right]GPP \tag{B-5}$$

where GPP denotes the gross primary production rate, $\overline{\overline{\alpha}}_{oc}$ is the ratio of oxygen to carbon for ammonia, $a_{NO_{3c}}$ is the ratio of oxygen to carbon for the nitrate uptake with a value of $\frac{48}{14}a_{NC}$, where a_{NC} is the ratio of nitrogen to carbon, defined as:

$$a_{NC} = \frac{\overline{\overline{QF}} + \left(1 - \overline{\overline{QF}}\right) \cdot u/u_{Pmax}}{\overline{\overline{W}}_{CN}} \tag{B-6}$$

Table 1
State variables in UG-RCA.

| Variable	Unit
Winter/spring phytoplankton	mg C l^{-1}
Summer phytoplankton	mg C l^{-1}
Fall phytoplankton	mg P l^{-1}
Particulate organic phosphorous—refractory component (RPOP)	mg P l^{-1}
Particulate organic phosphorous—labile component (LPOP)	mg P l^{-1}
Dissolved organic phosphorous—refractory component (RDOP)	mg P l^{-1}
Dissolved organic phosphorous—labile component (LDOP)	mg P l^{-1}
Total dissolved inorganic phosphorous	mg N l^{-1}
Particulate organic nitrogen—refractory component (RPON)	mg N l^{-1}
Particulate organic nitrogen—labile component (LPON)	mg N l^{-1}
Dissolved organic nitrogen—refractory component (RDON)	mg N l^{-1}
Dissolved organic nitrogen—labile component (LDON)	mg N l^{-1}
Total ammonia (ammonia in water and phytoplankton cell)	mg N l^{-1}
Nitrite + nitrate	mg Si l^{-1}
Biogenic silica	mg Si l^{-1}
Total silica—(silica in water and phytoplankton cell)	mg C l^{-1}
Particulate organic carbon—refractory component (RPOC)	mg C l^{-1}
Particulate organic carbon—labile component (LPOC)	mg C l^{-1}
Dissolved organic carbon—refractory component (RDOC)	mg C l^{-1}
Dissolved organic carbon—labile component (LDOC)	mg C l^{-1}
Dissolved organic carbon—algal exudate	mg C l^{-1}
Dissolved organic carbon—reactive component (ReDOC)	mg C l^{-1}
Particulate organic carbon—reactive component (RePOC)	mg C l^{-1}
O2*—aqueous oxygen	mg O$_2$ l^{-1}
Dissolved oxygen	mg O$_2$ l^{-1}

where $\overline{\overline{QF}}$ is the quotient of nutrient limited N:C ratio and $\overline{\overline{W}}_{CN}$ is the ratio of non-nitrogen-limited carbon to nitrogen. α_{NH_4}, the ammonia preference factor for phytoplankton uptake, is defined as:

$$\alpha_{NH_4} = NH_4 \cdot \frac{NO_2 + NO_3}{\left(\overline{\overline{k}}_{mN} + NH_4\right) \cdot \left(\overline{\overline{k}}_{mN} + NO_2 + NO_3\right)} \\ + NH_4 \cdot \frac{\overline{\overline{k}}_{mN}}{\left(\overline{\overline{k}}_{mN} + NH_4\right) \cdot \left(NH_4 + NO_2 + NO_3\right)} \tag{B-7}$$

where $\overline{\overline{k}}_{mN}$ is the Michaelis value (see Table 2). GPP is given as

$$GPP = \left(u + k_{pr}\right) \cdot P_c \tag{B-8}$$

where P_c is phytoplankton biomass. k_{pr} is phytoplankton endogenous respiration:

$$k_{pr} = \frac{\overline{\overline{k}}_{rb} + \overline{\overline{k}}_{rg} \cdot u}{1 - \overline{\overline{k}}_{rg}} \tag{B-9}$$

where $\overline{\overline{k}}_{rb}$ and $\overline{\overline{k}}_{rg}$ are basal respiration rate and growth-rate-dependent respiration rate. u is the phytoplankton net growth rate, defined as

$$u = u_{Pmax}\left(\overline{\overline{T}}_{opt}, I\right) \cdot G_t(T) \cdot G_n(N) \tag{B-10}$$

and $u_{Pmax}\left(\overline{\overline{T}}_{opt}, I\right)$ is the nutrient-saturated growth rate under optimal temperature $\overline{\overline{T}}_{opt}$, $G_t(T)$ is the temperature correction factor, and $G_n(N)$ is a nutrient limitation factor. They are calculated mathematically by:

$$u_{Pmax}\left(\overline{\overline{T}}_{opt}, I\right) = \frac{\overline{\overline{G}}_{prd} \cdot \left(1 - \overline{\overline{k}}_{rg}\right) \cdot \left(1 - \overline{\overline{F}}_{sc}\right) \cdot I(z,t)}{\overline{\overline{G}}_{prd}/\overline{\overline{G}}_{prlo} + I(z,t) \cdot \left(1 + \overline{\overline{G}}_{prd}/I_s \cdot \overline{\overline{G}}_{prlo}\right)} \tag{B-11}$$

$$\overline{\overline{G}}_t(T) = \exp\left(-\overline{\overline{\beta}}_1 \cdot \left(T - \overline{\overline{T}}_{opt}\right)\right) if \left(T \leq \overline{\overline{T}}_{opt}\right) \tag{B-12}$$

$$\overline{\overline{G}}_t(T) = \exp\left(-\overline{\overline{\beta}}_2 \cdot \left(T - \overline{\overline{T}}_{opt}\right)\right) if \left(T \geq \overline{\overline{T}}_{opt}\right) \tag{B-13}$$

$$G_n(N) = \min\left(\frac{DIN}{\overline{\overline{K}}_{mN} + DIN}, \frac{DIP}{\overline{\overline{K}}_{mP} + DIP}, \frac{S_i}{\overline{\overline{K}}_{mS_i} + S_i}\right) \tag{B-14}$$

where parameters $\overline{\overline{G}}_{prd}$, is the gross photosynthetic rate associated with dark reaction, $\overline{\overline{G}}_{prlo}$ gross photosynthetic rate per unit light intensity in the limit of zero irradiance, and $\overline{\overline{F}}_{sc}$ is the fraction of carbon allocated

Table 2
Parameters specified to the DO calculation in the UG-RCA.

Notation	Parameter definition	Value			Unit
		Winter/Spring group	Summer group	Fall group	
$\overline{\overline{T}}_{opt}$	Optimal growth temperature for algal group	8.0	18.0	14.0	°C
$\overline{\overline{\beta}}_1$	Temperature correction coefficient on growth rate below $\hat{T}_{opt}$	0.004	0.004	0.004	°C^{-2}
$\overline{\overline{\beta}}_2$	Temperature correction coefficient on growth rate above $\hat{T}_{opt}$	0.006	0.006	0.006	°C^{-2}
$\overline{\overline{k}}_{mN}$	Half-saturation constant for nitrogen uptake	0.010	0.010	0.005	mg N l^{-1}
$\overline{\overline{k}}_{mP}$	Half-saturation constant for phosphorous uptake	0.001	0.001	0.001	mg P l^{-1}
$\overline{\overline{k}}_{mSi}$	Half-saturation constant for silica uptake	0.020	0.005	0.004	mg Si l^{-1}
$\overline{\overline{G}}_{prd}$	Gross photosynthetic rate (associated with photosynthetic dark reaction)	2.5	3.0	2.5	d^{-1}
$\overline{G}_{prlo}$	Gross photosynthetic rate per unit cell per unit light intensity under nutrient saturated conditions and zero irradiance	0.64	0.64	0.64	m^2 Ein^{-1}
$\overline{\overline{k}}_{rb}$	Basal or resting respiration rate	0.030	0.036	0.030	d^{-1}
$\overline{\overline{k}}_{rg}$	Growth-rate-dependent respiration coefficient	0.28	0.28	0.28	
$\overline{\overline{F}}_{sc}$	Fraction of carbon allocated to structural purposes	0.1	0.1	0.1	
$\overline{\overline{k}}_{e_{base}}$	Background light extinction coefficient (2-D parameter)	0.16–0.6	0.16–0.6	0.16–0.6	m^{-1}
$\overline{\overline{k}}_c$	Phytoplankton self-shading coefficient	0.017	0.017	0.017	m^2(mg chl-a)$^{-1}$
$\overline{W}_{cchl}$	Nutrient-saturated carbon to chlorophyll ratio	40.0	65.0	15.0	mg C (mg chl)$^{-1}$
$\overline{\overline{k}}_{nit}$	Nitrification rate at 20 °C	0.1			d^{-1}
$\overline{\overline{\theta}}_{nit}$	Temperature correction coefficient for nitrification	1.080			
$\overline{\overline{k}}_{nit_{DO}}$	Half-saturation constant of oxygen limitation for nitrification	1.0			mg O$_2$ l^{-1}
$\overline{\overline{K}}_{m_{Pc}}$	Half saturation constant for phytoplankton	0.05			mg C l^{-1}
$\overline{\overline{K}}_{DO}$	Half-saturation constant for oxygen limitation	0.2			mg O$_2$ l^{-1}
$\overline{\overline{\theta}}_a$	Coefficient of temperature adjustment for reaeration	1.024			
$\overline{\overline{a}}_{oc}$	Oxygen to carbon ratio for ammonia	32/12			mgO$_2$ (mg C)$^{-1}$
$\overline{\overline{QF}}$	Quotient of nutrient limited N:C ratio	0.85			
$\overline{W}_{CN}$	Carbon to nitrogen ratio (non-nitrogen-limited)	5.67			mg C (mg N)$^{-1}$
$\overline{k}_{RDOC}$	Oxidation rate for RDOC at 20 °C	0.008			d^{-1}
$\overline{\theta}_{RDOC}$	Temperature correction coefficient for RDOC oxidation	1.080			
$\overline{k}_{LDOC}$	Oxidation rate for LDOC	0.1			d^{-1}
$\overline{\theta}_{LDOC}$	Temperature correction coefficient for LDOC oxidation	1.080			
$\overline{k}_{m_{LDOC}}$	Michaelis constant for LDOC	0.100			mg C l^{-1}
$\overline{k}_{R_eDOC}$	Oxidation rate for ReDOC at 20 °C	0.300			d^{-1}
$\overline{\theta}_{R_eDOC}$	Temperature correction coefficient for ReDOC oxidation	1.047			
$\overline{k}_{E_xDOC}$	Oxidation rate for exudate DOC at 20 °C	0.125			d^{-1}
$\overline{\theta}_{E_xDOC}$	Temperature correction coefficient for Exudate DOC oxidation	1.08			
$\overline{K}_{m_{LDOC}}$	Michaelis constant for LDOC	0.1			mg C l^{-1}
$\overline{a}_{ON}$	Oxygen to nitrogen ratio	32/14			
$\overline{k}_{o_2}$	Oxidation rate of dissolved sulfide at 20 °C	0.15			d^{-1}
$\overline{\theta}_{o_2}$	Temperature correction coefficient for the oxidation of dissolved sulfide	1.08			
$\overline{K}_{DO_{o2}}$	Half-saturation constant of oxygen limitation for dissolved sulfide	0.2			mg O$_2$ l^{-1}

to structural purposes, respectively. $\overline{\overline{\beta}}_1$ and $\overline{\overline{\beta}}_2$ are the coefficients of the temperature correction effect on growth rate below and above optimal temperature $\overline{\overline{T}}_{opt}$. $\overline{\overline{K}}_{mN}$, $\overline{\overline{K}}_{mP}$ and $\overline{\overline{K}}_{mSi}$ are the half-saturation constants for nitrogen, phosphorous and silica uptake, respectively. $I(z,t)$ is the light attenuation function given as

$$I(z,t) = I_{surf}(t)e^{-k_e z} \qquad (B-15)$$

where k_e being defined as the total light extinction coefficient:

$$k_e = \overline{\overline{k}}_{e_{base}} + \overline{\overline{k}}_c \cdot a_{chlc} \cdot P_c \qquad (B-16)$$

$\overline{\overline{k}}_{e_{base}}$ and $\overline{\overline{k}}_c$ are background light extinction coefficient and phytoplankton self-shading coefficient, and chlorophyll to carbon ratio a_{chlc} is calculated as:

$$a_{chlc} = \frac{1 - \left(1 - \overline{QF}\right)\left(1 - \frac{u}{u_{Pmax}}\right) - \overline{\overline{F}}_{sc} - \left(u + \overline{\overline{k}}_{rb}\right) / \left[\left(1 - \overline{\overline{k}}_{rg}\right)\overline{G}_{prd}\right]}{\overline{W}_{cchl}} \qquad (B-17)$$

where $\overline{W}_{cchl}$ is the ratio of nutrient-saturated carbon to chlorophyll.

The surface solar radiation $I_{surf}(t)$ being calculated from daily mean solar radiation I_{tot}, time of day t_d, time of sunrise $t_{sunrise}$ and fraction of daylight f:

$$I_{surf}(t) = \frac{I_{tot}}{0.635 f} \sin\left(\frac{\pi(t_d - t_{sunrise})}{f}\right) \qquad (B-18)$$

$$I_s = \left(I_{tot_{n-1}} + I_{tot_{n-2}} + I_{tot_{n-3}}\right). \qquad (B-19)$$

DIN = dissolved inorganic nitrogen = $NH_3 + NO_2 + NO_3$, DIP = dissolved inorganic phosphorus, and S_i = available silica.

The phytoplankton respiration (F_{resp}) is calculated by

$$F_{resp} = \overline{\overline{a}}_{oc} \cdot k_{pr} \cdot P_c. \qquad (B-20)$$

Oxidation of organic matter (F_{oxid}) is determined by the organic carbon fluxes from phytoplankton, including the reactive organic carbon (ReDOC), exudated organic carbon (ExDOC), labile organic carbon (LDOC) and refractory organic carbon (RDOC). The formulae used to calculate this term is given as

$$F_{oxid} = \overline{\overline{\alpha}}_{oc} \cdot \left[\overline{k}_{RDOC}^{DO} \cdot \overline{\theta}_{RDOC}^{DO} \cdot RDOC + \overline{k}_{LDOC}^{DO} \cdot LDOC \cdot \frac{LDOC}{\overline{K}_{m_{LDOC}} + LDOC} + \overline{k}_{R_eDOC}^{DO} \cdot \overline{\theta}_{R_eDOC}^{DO} \cdot R_eDOC \cdot \frac{R_eDOC}{\overline{K}_{m_{LDOC}} + R_eDOC} + \overline{k}_{E_xDOC}^{DO} \cdot \overline{\theta}_{E_xDOC}^{DO} \cdot E_xDOC \cdot \frac{E_xDOC}{\overline{K}_{m_{LDOC}} + E_xDOC}\right] \cdot \frac{P_c}{\overline{\overline{K}}_{m_{Pc}} + P_c} \cdot \frac{DO}{\overline{\overline{K}}_{DO} + DO} \qquad (B-21)$$

where $\overline{k}_{RDOC}^{DO}$, $\overline{k}_{LDOC}^{DO}$, $\overline{k}_{R_eDOC}^{DO}$ and $\overline{k}_{E_xDOC}^{DO}$ are oxidation rates at 20 °C for RDOC, LDOC, ReDOC and ExDOC, respectively. $\overline{\theta}_{RDOC}$, $\overline{\theta}_{LDOC}$, $\overline{\theta}_{R_eDOC}$, and $\overline{\theta}_{E_xDOC}$ are temperature correction coefficients. $\overline{K}_{m_{LDOC}}$ is the Michaelis constant for LDOC, $\overline{\overline{K}}_{m_{Pc}}$ and $\overline{\overline{K}}_{DO}$ are half-saturation constants of phytoplankton and oxygen limitation, respectively.

Nitrification (F_{nit}) is simply the conversion of nitrate generation from nitrification with the ratio $\bar{\bar{a}}_{ON}$ of oxygen to nitrogen given as

$$F_{nit} = 2 \cdot \bar{\bar{a}}_{ON} \cdot \bar{\bar{k}}_{nit} \cdot \bar{\bar{\theta}}_{nit}^{T-20} \cdot NH_4 \cdot \frac{DO}{\bar{\bar{k}}_{nit_{DO}} + DO} \qquad (B-22)$$

where $\bar{\bar{k}}_{nit}$ is the nitrification rate at 20 °C, $\bar{\bar{\theta}}_{nit}$ is the temperature correction coefficient for nitrification and $\bar{\bar{k}}_{nit_{DO}}$ is the half-saturation constant of oxygen limitation for nitrification.

Sulfide oxygen equivalents ($F_{sulfide}$) are defined as

$$F_{sulfide} = \bar{\bar{k}}_{o_2^*} \cdot \bar{\bar{\theta}}_{o_2^*}^{T-20} \cdot O_2^* \cdot \frac{P_c}{\bar{\bar{K}}_{m_{P_c}} + P_c} \cdot \frac{DO}{\bar{\bar{K}}_{DO_2^*} + DO} \qquad (B-23)$$

where $\bar{\bar{k}}_{o_2^*}$ is the oxidation rate of dissolved sulfide at 20 °C, $\bar{\bar{\theta}}_{o_2^*}$ is the temperature correction coefficient for dissolved sulfide, $\bar{\bar{K}}_{DO_2^*}$ are a half-saturation constant of oxygen limitation for dissolved sulfide.

Oxygen used by SOD is calculated by an entire UG-RCA sediment module based on mass transfer formula

$$D_1 \left. \frac{d(O_2)}{dz} \right|_{z=bottom}, \qquad (B-24)$$

where D_1 is the diffusion function in the sediment layer and $\frac{d(O_2)}{dz}$ is the DO gradient from aerobic sediment depth to the water column above the sediment. We were focused on the dissolved oxygen in the water, so that we only took the output from SOD as a sink term in our DO balance. For details of the SOD process, we refer interested readers to the *User's guide for RCA* (HydroQual, Inc., 2004).

References

Anderson, D.M., Keafer, B.A., McGillicuddy, D.J., Mickelson, M.J., Keay, K.E., Libby, P.S., Manning, J.P., Mayo, C.A., Whittaker, D.K., Hickey, J.M., He, R., Lynch, D.R., Smith, K.W., 2005. Initial observations of the 2005 *Alexandrium fundyense* bloom in southern New England: general patterns and mechanisms. Deep-Sea Res. II 5219–21, 2856–2876.

Anderson, D.M., Libby, P.S., Mickelson, M.J., Borkman, D.G., McGillicuddy, D.J., 2007. The 2005 New England red tide of *Alexandrium fundyense*: observations, causes, and potential outfall linkages. Report 2007–10Massachusetts Water Resources Authority, Boston (85 pp.).

Bigelow, H.B., 1927. Physical oceanography of the Gulf of Maine (part II). Bull. Bur. Fish. 40, 511–1027.

Blumberg, A.F., 1994. A Primer for ECOM-si. Technical Report. HydroQual, Inc., Mahwah, New Jersey (101 pp.).

Chen, C., Beardsley, R.C., Cowles, G., 2006a. An unstructured grid, finite-volume coastal ocean model (FVCOM) system, Special Issue entitled "Advances in Computational Oceanography". Oceanography 19 (1), 78–89.

Chen, C., Cowles, G., Beardsley, R.C., 2006b. An unstructured grid, finite-volume coastal ocean model: FVCOM user manual, SMAST/UMASSD Technical Report-06-0602 Second edition. 315.

Chen, C., Liu, H., Beardsley, R., 2003. An unstructured grid, finite-volume, three dimensional, primitive equations ocean model: application to coastal ocean and estuaries. J. Atmos. Oceanic Tech. 20 (1), 159–186.

Chen, C., Tian, R., Beardsley, R., Qi, J., Xu, Q., 2010. Modeling 2008 in Massachusetts Bay using an upgraded unstructured-grid Bays Eutrophication Model. Report 2010–15. Massachusetts Water Resources Authority, Boston (128 pp.).

Geyer, W.R., Libby, L., Giblin, A., 2002. Influence of physical controls on dissolved oxygen variation at the outfall site. Letter Report.Massachusetts Water Resources Authority, Boston (20 pp.).

Geyer, W.R., Gardner, G.B., Brown, W.S., Irish, J., Butman, B., Loder, T., Signell, R.P., 1992. Physical oceanographic investigation of Massachusetts and Cape Cod Bays, Rep. MBP-92-03. Mass. Bay Program, Boston, Mass (497 pp.).

Hendry, R., He, I., 1996. Technical Report on Objective Analysis (OA) Project. Bedford Institute of Oceanography, Dartmouth, Nova Scotia (105 pp.).

HydroQual, Inc., 2004. User's Guide for RCA Release 3.0 (200 pp.).

HydroQual, Inc., Normandeau Associates, 1995. A water quality model for Massachusetts and Cape Cod Bays: calibration of the bays eutrophication model. Technical Report ENQUAD 95–08.Massachusetts Water Resources Authority, Boston, MA (402 pp.).

HydroQual, Inc., 2003. Bays Eutrophication Model (BEM): Modeling Analysis for the Period 1998–1999, Rep. ENQUAD 2003–03. Massachusetts Water Resources Authority, Boston, MA (18 pp.).

Hunt, C.D., Borkman, D.G., Libby, P.S., Lacouture, R., Turner, J.T., Mickelson, M.J., 2010. Phytoplankton patterns in Massachusetts Bay—1992–2007. Estuar. Coasts. http://dx.doi.org/10.1007/s12237-008-9125-9.

Jiang, M.S., Zhou, M., 2004. Calibration of the Massachusetts and Cape Cod Bays Water Quality Model: 2000– 2001, Rep. ENQUAD 2004–09. Massachusetts Water Resources Authority, Boston, MA.

Jiang, M.S., Wallace, G.T., Zhou, M., Libby, S., Hunt, C.D., 2007. Summer formation of a high-nutrient low-oxygen pool in Cape Cod Bay, USA. J. Geophys. Res. 112, C05006. http://dx.doi.org/10.1029/2006JC003889.

Kelly, J.R., Doering, P.H., 1999. Seasonal deepening of the pycnocline in a shallow shelf ecosystem and its influence on near-bottom dissolved oxygen. Mar. Ecol. Prog. Ser. 178, 151–168.

Lagerloef, G.S.E., Bernstein, R.L., 1988. Empirical orthogonal function analysis of Advanced Very High Resolution Radiometer surface temperature patterns in Santa Barbara Channel. J. Geophys. Res. 93, 6863–6873.

Libby, P.S., Geyer, W.R., Keller, A.A., Turner, J.T., Borkman, D., Oviatt, C.A., Hunt, C.D., 2003. 2002 Annual Water Column Monitoring Report, Report 2003–09. Massachusetts Water Resources Authority, Boston, MA (111 pp.).

Libby, P.S., Geyer, W.R., Keller, A.A., Turner, J.T., Borkman, D., Oviatt, C.A., 2004. 2003 Annual Water Column Monitoring Report, Report 2004–07. Massachusetts Water Resources Authority, Boston, MA (154 pp.).

Libby, P.S., Geyer, W.R., Keller, A.A., Mansfield, A.D., Turner, J.T., Anderson, D.M., Borkman, D.G., Rust, S., Hyde, K., Oviatt, C.A., 2007. Water Column Monitoring in Massachusetts Bay: 1992–2006, Report 2007–11. Massachusetts Water Resources Authority, Boston, MA (228 pp.).

Maciolek, N.J., Dahlen, D.T., Diaz, R.J., 2009. 2008 Boston Harbor Benthic Monitoring Report, Report 2009–14. Massachusetts Water Resources Authority, Boston, MA (19 pp.).

Mellor, G.L., Yamada, T., 1982. Development of a turbulence closure model for geophysical fluid problem. Rev. Geophys. Space Phys. 20, 851–875.

Oviatt, C.A., Hyde, K.J.W., Keller, A.A., Turner, J.T., 2007. Production patterns in Massachusetts Bay with outfall relocation. Estuar. Coasts 30, 35–46.

Pietrzak, J.J.B., Jakobson, H., Burchard, H., Vested, H.J., Petersen, O., 2002. A three-dimensional hydrostatic model for coastal and ocean modeling using a generalized topography following co-ordinate system. Ocean Model. 4, 173–205.

Preisendorfer, R.W., 1988. Principal Component Analysis in Meteorology and Oceanography. Elsevier, New York (425 pp.).

Reback, K.E., Brady, P.D., McLauglin, K.D., Milliken, C.G., 2004. A survey of anadromous fish passage in coastal Massachusetts: Part 1–4. Massachusetts Division of Marine Fisheries Technical Report TR-15.

Signell, R.P., Jenter, H.L., Blumberg, A.F., 2000. Predicting the physical effects of relocating Boston's sewage outfall. J. Estuar. Coast. Shelf. Sci. 50, 59–72.

Smagorinsky, J., 1963. General circulation experiments with the primitive equations, I. The basic experiment. Mon. Weather Rev. 91, 99–164.

Tian, R., Chen, C., Xu, Q., Xue, P., Cowles, G., Beardsley, R., Rothschild, B., 2009. The Massachusetts Bay Water Quality Model: 2006–2007 Simulation, Report 2009–11. Massachusetts Water Resources Authority, Boston, MA (124 pp.).

Tian, R., Chen, C., Zhao, L., Xue, P., Leo, W., Mickelson, M., 2010. Modeling 2009 in Massachusetts Bay Using the Unstructured-grid Bays Eutrophication Model, Report 2010–22. Massachusetts Water Resources Authority, Boston, MA (100 pp.).

Tucker, J., Kelsey, S., Giblin, A., Hopkinson, C., 2008. 2007 Annual Benthic Nutrient Flux Monitoring Report, Report ENQUAD 2008–14. Massachusetts Water Resources Authority, Boston, MA (59 pp.).

Xue, P., Chen, C., Beardsley, R.C., 2012. Observing System Simulation Experiments (OSSEs) of dissolved oxygen monitoring in Massachusetts Bay. J. Geophys. Res. http://dx.doi.org/10.1029/2011JC007843.

Zhao, L., Tian, R., Xue, P., Chen, C., Leo, W., Mickelson, M., 2011. Modeling 2010 in Massachusetts Bay Using the Unstructured-grid Bays Eutrophication Model, Report 2011–09. Massachusetts Water Resources Authority, Boston, MA (118 pp.).